

1 **Abiotic methane generation through reduction of serpentinite-hosted**
2 **dolomite: implications for carbon mobility in subduction zones**

3 Weigang Peng^{a,b,c}, Lifei Zhang^{a,*}, Simone Tumiati^c,

4 Alberto Vitale Brovarone^{d,e}, Han Hu^a, Yachun Cai^b, Tingting Shen^f

5 ^a *MOE Key Laboratory of Orogenic Belts and Crustal Evolution, School of Earth*
6 *and Space Sciences, Peking University, Beijing 100871, China*

7 ^b *Deep Sea Research Center, Pilot National Laboratory for Marine Science and*
8 *Technology (Qingdao), Qingdao 266061, China*

9 ^c *Dipartimento di Scienze della Terra, Università degli Studi di Milano, via*
10 *Mangiagalli 34, 20133 Milano, Italy*

11 ^d *Dipartimento di Scienze Biologiche, Geologiche e Ambientali, Alma Mater*
12 *Studiorum Università di Bologna, Piazza di Porta San Donato 1, 40126 Bologna,*
13 *Italy*

14 ^e *Sorbonne Université, Muséum National d'Histoire Naturelle, UMR CNRS 7590,*
15 *IRD, Institut de Minéralogie, de Physique des Matériaux et de Cosmochimie,*
16 *IMPMC, 4 Place Jussieu, 75005 Paris, France*

17 ^f *Institute of Geology, Chinese Academy of Geological Sciences, Beijing 100037,*
18 *China*

19
20 *Corresponding author: Lifei Zhang

21 E-mail: lfzhang@pku.edu.cn

22 Telephone: +86-010-62751145

23 **ABSTRACT**

24 Abiotic methane has been increasingly detected at the surface of Earth and
25 other terrestrial planets, exerting a strong effect on the study of
26 chemolithoautotrophic life and thus astrobiology. In contrast, abiotic methane
27 generation in subduction zones, which is intimately linked to questions such as
28 the mechanisms of deep carbon mobility, has received scarce attention.
29 Experiments elucidated the significant production of abiotic methane through
30 reduction of carbonate minerals under subduction zone conditions, whereas
31 detailed geological conditions and processes for the reduction in natural rocks are
32 hitherto poorly understood. Here, we report carbonate reduction and genesis of
33 abiotic methane in dolomitized serpentinites (referred to as ophidolomites) from
34 a fossil subduction zone (SW Tianshan, China). Detailed petrological, Raman
35 spectroscopic, strontium and carbon isotopic, and thermodynamic results provide
36 evidence for dolomite reduction into the phase assemblage of calcite + brucite +
37 methane, likely associated with retrograde serpentinization starting at 7–9 kbar
38 and 410–430 °C in the subduction zone. Microthermometric data for dolomite-
39 hosted fluid inclusions are consistent with petrographic observations, indicative
40 of fluid entrapment postdating the onset of dolomite reduction during exhumation.
41 Model calculations suggest that water-rich fluids characterized by relatively high
42 hydrogen fugacities can create favorable conditions for the reduction process,
43 which, however, do not exclude the possibility of carbonate methanation by
44 hydrogen-rich fluids as reported in previous studies. The widespread occurrence

45 of methane in these rocks gives credence to the intricate redox transformations of
46 subducted carbon, implying that the elevated hydrogen fugacities may facilitate
47 abiotic synthesis of methane through dolomite reduction at convergent plate
48 boundaries. Our work shows that alteration of dolomite-bearing lithologies
49 represents a potential source for abiotic methane in subduction zones, which may
50 have implications for the transfer of subducted carbon.

51

52 *Keywords:* Abiotic methane; Dolomite reduction; Ophicarbonate; Hydrogen
53 fugacity; Subduction zone; Chinese southwestern Tianshan

54

55 **1. INTRODUCTION**

56 Redox transformations in subduction zones regulate the valence of carbon
57 (C), and thus control the long-term fate of subducted C (e.g., [Hayes and](#)
58 [Waldbauer, 2006](#); [Evans, 2012](#); [Galvez and Pubellier, 2019](#); [Tumiati and](#)
59 [Malaspina, 2019](#); [Sheik et al., 2020](#)). Carbonation of subduction-zone rocks at
60 forearc to subarc depths by interactions with slab-derived carbon dioxide (CO₂)-
61 bearing fluids gives insights into C sequestration under oxidized conditions
62 ([Tumiati et al., 2013](#); [Piccoli et al., 2016, 2018](#); [Scambelluri et al., 2016](#); [Jaeckel](#)
63 [et al., 2018](#); [Sieber et al., 2018, 2020](#); [Peng et al., 2020](#); [Hu et al., 2021](#)). On the
64 other hand, reduction of carbonate minerals at convergent plate boundaries
65 generates graphite and/or hydrocarbons such as methane (CH₄), modulating the
66 distribution of subducted C between solid and fluid inventories ([Malvoisin et al.,](#)

67 2012; Galvez et al., 2013a, b; Vitale Brovarone et al., 2017; Tao et al., 2018a;
68 Giuntoli et al., 2020). Graphite formation through carbonate reduction during
69 shallow subduction offers a potential mechanism to retain C in subducted slabs,
70 which may facilitate C transport into the deep Earth (Malvoisin et al., 2012;
71 Galvez et al., 2013a, b). In contrast, the release of CH₄ from subducted
72 ophicalcites (Western Alps, Italy; Vitale Brovarone et al., 2017; Giuntoli et al.,
73 2020) and carbonated eclogites (SW Tianshan, China; Tao et al., 2018a),
74 attributed to hydrogen (H₂)-induced reduction of calcite (referred to as carbonate
75 methanation; Etiope and Sherwood Lollar, 2013 and references therein) and
76 aqueous reduction of ferroan dolomite, respectively, provides evidences for
77 mobile deep C reservoirs. Moreover, olivine-hosted secondary CH₄-bearing fluid
78 inclusions were observed in partially serpentized rocks within and above
79 subducted slabs, interpreted as being due to the reduction of C-bearing species in
80 metamorphic fluids through subduction-zone serpentization (Sachan et al., 2007;
81 Vitale Brovarone et al., 2020; Boutier et al., 2021). Therefore, investigating
82 mechanisms for abiotic CH₄ generation in subduction zones is helpful to our
83 comprehension of the transfer of slab C.

84 Abiotic CH₄ has been increasingly identified during the past decades,
85 particularly at shallow geodynamic settings (such as in mid-ocean ridge
86 hydrothermal systems; e.g., Kelley et al., 2001, 2005), revealing its more
87 extensive distribution than conventionally assumed (Etiope and Sherwood Lollar,
88 2013; Etiope and Schoell, 2014). In submarine environments, the hydration of

89 exposed mantle rocks (referred to as serpentinization) commonly accompanies H₂
90 discharge, which may favor the synthesis of abiotic CH₄—with or without other
91 short-chain hydrocarbons, such as ethane (C₂H₆), propane (C₃H₈), and butane
92 (C₄H₁₀)—via Fischer–Tropsch-type reduction of aqueous CO₂ in seawater (e.g.,
93 [Charlou et al., 2002, 2010](#); [Proskurowski et al., 2008](#)). Conversely, several
94 metastable intermediate species (e.g., formates), instead of light hydrocarbons,
95 have been considered to be predominantly generated by abiotic reduction of
96 dissolved inorganic C during seawater circulation through ultramafic rocks in the
97 subsurface ([McCollom et al., 2001](#); [McDermott et al., 2015](#)). Geological
98 production of these organic compounds plays a potential role in the origin of
99 chemolithoautotrophic life on Earth and other terrestrial planets (e.g., [McCollom
100 and Seewald, 2013](#); [McDermott et al., 2015](#); [Ménez, 2020](#); [Truche et al., 2020](#)).
101 Furthermore, H₂-induced reduction of C-bearing species by serpentinization
102 within olivine-hosted fluid inclusions in submarine and subaerial vent systems
103 likely represents a widespread reservoir of abiotic CH₄ over geological timescales
104 ([Klein et al., 2019](#); [Grozeva et al., 2020](#)). In contrast, abiotic formation of CH₄ in
105 subduction zones, which is closely related to the mechanisms of deep C mobility,
106 has received scarce attention. Experiments demonstrated that abiotic CH₄ can be
107 generated under subduction zone conditions through reduction of subducted C
108 (e.g., carbonate minerals, organic matter, and dissolved aqueous organic species;
109 [Sharma et al., 2009](#); [Lazar et al., 2014](#); [Huang et al., 2017](#); [Li, 2017](#); [Mukhina et
110 al., 2017](#); [Tao et al., 2018a](#)). However, the manifestations of abiotic CH₄ in natural

111 subduction-zone rocks, as well as the geological conditions and reaction pathways
112 for its production, have been paid insufficient attention, even though CH₄-bearing
113 fluid inclusions are not particularly rare in metamorphic lithologies within and
114 above subducted slabs (Shi et al., 2005; Sachan et al., 2007; Song et al., 2009;
115 Arai et al., 2012; Vitale Brovarone et al., 2017, 2020; Tao et al., 2018a; Giuntoli
116 et al., 2020; Boutier et al., 2021; Zhang et al., 2021).

117 In this contribution, we report dolomite reduction and genesis of abiotic CH₄
118 in ophidolomites belonging to the ultramafic unit of Changawuzi in the Chinese
119 southwestern Tianshan high-pressure–ultrahigh-pressure (HP–UHP)
120 metamorphic belt. We show and discuss petrology, Raman spectroscopy,
121 microthermometry, strontium (Sr) and C isotope geochemistry, and
122 thermodynamic modelling to improve understanding of abiotic CH₄ generation in
123 subduction zones.

124

125 2. GEOLOGICAL BACKGROUND AND SAMPLES

126 The Chinese southwestern Tianshan HP–UHP metamorphic belt is located
127 in the northwest of China and formed due to northward subduction of the Tarim
128 Plate underneath the Yili–Central Tianshan Plate (Fig. 1A; Zhang et al., 2013).
129 The spatial distribution of HP–UHP rocks in this metamorphic belt allows the
130 subdivision of a southern HP sub-belt and a northern, coesite-bearing, UHP sub-
131 belt (Fig. 1B; Lü and Zhang, 2012; Lü et al., 2012a, b; Zhang et al., 2013). The
132 current work focuses on the Chinese southwestern Tianshan UHP metamorphic

133 belt, which mainly experienced (1) UHP metamorphism (~30 kbar and ~500 °C)
134 at ca. 320 Ma, (2) peak temperature metamorphism at HP conditions during
135 exhumation (i.e., thermal relaxation; ~22 kbar and ~600 °C) at ca. 310–315 Ma,
136 and (3) multistage exhumation to relatively shallow depths (from eclogite facies
137 to greenschist facies) (Tan et al., 2017; Zhang et al., 2019 and references therein).

138 The main rock types in the Chinese southwestern Tianshan HP–UHP
139 metamorphic belt are garnet–phengite schists, marbles, blueschists, eclogites, and
140 serpentinites with associated rodingites (e.g., Shen et al., 2015). Serpentinites are
141 mostly exposed at Changawuzi in an area of about 6–10 km² (Fig. 1C), recording
142 two stages of serpentinization: (1) a seawater-related hydration process of oceanic
143 mantle rocks overprinted by the UHP metamorphism (37 ± 7 kbar and 520 ± 10
144 °C) during subduction (Shen et al., 2015) and (2) a later rehydration process of
145 metamorphic and/or primary olivine and pyroxene during exhumation (i.e.,
146 retrograde serpentinization) starting at 7–9 kbar and 410–430 °C and propagating
147 to lower *P–T* conditions (Li et al., 2007, 2010). Carbonated serpentinites,
148 including HP ophidolomites and low-pressure (LP) ophimagnesites and
149 listvenites, occur in association with the serpentinites and record two carbonation
150 processes that happened at different stages of exhumation from a depth of ~70 km
151 to relatively shallow crustal levels (Peng et al., 2020).

152 The herein studied CH₄-bearing ophidolomites are intimately associated with
153 (carbonated) serpentinites in the Changawuzi ultramafic blocks (Fig. 1C), which
154 are surrounded by mica schists (for detailed field occurrence, see Peng et al.,

155 2020). These ophidolomites are characterized by discontinuous and folded
156 dolomite veins hosted in serpentinites, in which dolomite is encircled by
157 yellowish calcite and brucite (Fig. 2A and B). Other than the studied samples at
158 Changawuzi, CH₄-bearing fluid inclusions were also reported in carbonated
159 eclogites in adjacent localities of Kebuerte and Habutengsu (Fig. 1B; Tao et al.,
160 2018a), indicating a relatively widespread distribution of CH₄ in the Chinese
161 southwestern Tianshan HP–UHP metamorphic belt.

162

163 3. METHODS

164 3.1. Scanning electron microscopic analyses

165 Back-scattered electron (BSE) images and compositional X-ray maps were
166 obtained using an FEI Quanta 650 FEG scanning electron microscope (SEM)
167 equipped with an Oxford INCA X-MAX50 250+ energy dispersive X-ray
168 spectrometer at the School of Earth and Space Sciences (SESS), Peking
169 University. The running conditions were set to an acceleration voltage of 10 kV,
170 a beam current of 5 nA, and a working distance of ~10 mm. Compositional X-ray
171 maps were recorded with an integration time of ~360 min.

172 3.2. Electron microprobe analyses

173 Mineral compositions were analyzed using a JEOL 8230 electron
174 microprobe analyzer at SESS, Peking University. The SPI 53 mineral standards
175 (U.S.) were adopted for the quantitative analyses (following Li et al., 2018):
176 jadeite for sodium (Na), aluminium (Al), and silicon (Si); rutile for titanium (Ti);

177 chromium oxide for chromium (Cr); hematite for iron (Fe); rhodonite for
178 manganese (Mn); diopside for magnesium (Mg) and calcium (Ca); sanidine for
179 potassium (K); and nickel silicide for nickel (Ni). The acceleration voltage and
180 beam current were 15 kV and 10 nA, respectively. The beam diameter was 2 μm
181 for all minerals except for calcite (5–10 μm). The PRZ correction was performed
182 at the final calibration stage.

183 **3.3. Raman spectroscopic and microthermometric analyses**

184 Raman spectra were acquired using a Renishaw InVia Reflex
185 microspectrometer at SESS, Peking University. Measurements were conducted
186 on polished thin sections (30 μm thick for mineral analyses and 100 μm thick for
187 fluid inclusion analyses) without any glue or resin. The laser (532 nm) was
188 focused on the sample by a DMLM Leica microscope with a 100-fold objective
189 (numerical aperture (N.A.) = 0.85). Different laser powers were set from an initial
190 50 mW source for opaque minerals (10%), silicates (50%–100%), carbonates
191 (50%–100%), and fluid inclusions (100%). The spectrometer was calibrated with
192 a synthetic Si wafer.

193 Fluid inclusion microthermometric studies were carried out using a Linkam
194 THMSG 600 heating–freezing stage mounted onto an Olympus microscope at
195 Key Laboratory of Mineral Resources, Institute of Geology and Geophysics,
196 Chinese Academy of Sciences (IGGCAS). The two-phase (vapor and liquid) fluid
197 inclusions with relatively large sizes were selected to determine the final ice
198 melting temperatures and homogenization temperatures. The heating rates of 0.1–

199 0.2 °C/min were adopted for the determination when phase transitions were
200 approached. The estimated errors in the measurements are ± 0.1 °C for the melting
201 temperatures and ± 2 °C for the homogenization temperatures. Salinities,
202 pressures at homogenization, and isochore slopes for the fluid inclusions were
203 calculated using the procedures described by [Steele-MacInnis et al. \(2012\)](#).

204 **3.4. *In situ* Sr isotopic analyses**

205 *In situ* Sr isotopic measurements of dolomite and calcite were performed by
206 Nu Plasma II MC-ICP-MS coupled with a 193-nm ArF excimer laser ablation
207 system (GeoLas HD) at SESS, Peking University (see [Lin et al., 2021](#) for detailed
208 description of the instrument and laser ablation system). Instrumental operating
209 conditions and data acquisition protocols are similar to those described in [Ramos](#)
210 [et al. \(2004\)](#) and [Yang et al. \(2009\)](#). The laser ablation was performed using a spot
211 size of ~ 90 μm , a repetition rate of ~ 5 Hz, and an energy density of ~ 10 J/cm².
212 The helium (He) gas (with a flow rate of ~ 0.5 L/min), carrying ablated sample
213 aerosols and passing through the “wire” signal smoothing device ([Hu et al., 2012](#)),
214 was merged with argon (Ar) gas before entering the plasma. Prior to each ablation,
215 a 30-s measurement of gas blank was employed to correct for the isobaric
216 interference of krypton (Kr). Correction of rubidium (Rb) was conducted using
217 the natural ratio of $^{85}\text{Rb}/^{87}\text{Rb} = 2.5926$ with an exponential law, assuming that the
218 mass bias of Rb is identical to that of Sr (e.g., [Woodhead et al., 2005](#)). Actually,
219 the studied samples have extremely low $^{87}\text{Rb}/^{86}\text{Sr}$ values, indicative of the
220 negligible interference of Rb. Previous studies have demonstrated that the

221 interference of Ca argides and dimers in carbonate minerals is minor and thus has
222 insignificant influence on the accuracy of $^{87}\text{Sr}/^{86}\text{Sr}$ ratios (e.g., [Ramos et al., 2004](#);
223 [Vroon et al., 2008](#); [Yang et al., 2009](#)). Double-charged ions in the samples have
224 extremely low ion signals, suggesting that they play a very limited role in
225 interfering $^{87}\text{Sr}/^{86}\text{Sr}$ ratios. The instrumental mass bias was corrected using the
226 $^{86}\text{Sr}/^{88}\text{Sr}$ ratio of 0.1194 with an exponential law. A modern Porites coral (Hainan
227 Island, China) was used as the internal standard to evaluate the accuracy of the
228 analyses, which yielded $^{87}\text{Sr}/^{86}\text{Sr}$ ratios of 0.709170 ± 0.000016 (2σ , $n = 33$), in
229 agreement with those obtained by solution-based MC-ICP-MS analyses ($^{87}\text{Sr}/^{86}\text{Sr}$
230 = 0.709176 ± 0.000016 ; [Yang et al., 2009](#)). In this study, Sr isotope data with
231 generally comparable ^{88}Sr ion signals higher than ~ 1 V were selected for dolomite
232 and calcite to minimize the potential influence of composition-induced matrix
233 effects and brucite interference on calcite due to their intergrown textures ([Section](#)
234 [4.1](#)). In general, the analyzed $^{87}\text{Sr}/^{86}\text{Sr}$ ratios of dolomite are close to those
235 obtained by solution-based TIMS analyses for dolomite in surrounding HP
236 ophidolomites ([Section 4.3](#); [Peng et al., 2020](#)).

237 **3.5. C and O isotopic analyses**

238 Microdrilling was conducted on dolomite and calcite using a standard dentist
239 drill (0.2 mm, 0.5 mm, and 1.0 mm) under the stereomicroscope (SMZ 1500) at
240 State Key Laboratory of Lithospheric Evolution (SKLLE), IGGCAS. Vertical
241 holes were drilled down to thick sections (ca. 0.3–0.5 mm) by increments and at
242 least 2 mg of powder of each selected grain was collected. C and O isotope

243 compositions of dolomite, calcite, and bulk carbonate were determined using a
244 Thermo Fisher MAT 253 isotope ratio mass spectrometer coupled with a
245 GasBench II peripheral device at SKLLE, IGGCAS, through production of CO₂
246 after reaction with phosphoric acid. The reaction vial was automatically flushed
247 with high-purity (99.999%) He gas for 10 min at a flow rate of ~0.1 L/min to
248 remove atmospheric contaminants including traces of CO₂ and water (H₂O) vapor.
249 The acid digestion was performed in the GasBench II using continuous flow mode
250 at a temperature of 70 °C, through which the generated CO₂ was transferred by
251 the He carrier gas into the mass spectrometer. In the analyses, δ¹⁸O values of bulk
252 carbonate were not reported because the mixture of dolomite and calcite prevents
253 the accurate back-calculation by using O isotope fractionation factors between the
254 carbonate and phosphoric acid. Standard deviations of δ¹³C and δ¹⁸O values were
255 calculated from replicate analyses of an internal laboratory calcite standard, which
256 are better than 0.15‰ and 0.20‰, respectively. The measured δ¹³C and δ¹⁸O
257 values are reported relative to the Vienna Pee Dee Belemnite (V-PDB) and
258 Vienna Standard Mean Ocean Water (V-SMOW), respectively.

259 **3.6. Thermodynamic modelling**

260 To evaluate the role of oxygen fugacity (fO_2 ; log bar unit) and hydrogen
261 fugacity (fH_2 ; log bar unit) in the reduction process of dolomite (nearly pure;
262 [Section 4.1](#)), we calculated the fO_2 – fH_2 equilibrium diagram in the Ca–Mg–C–O–
263 H system (with fixed Ca:Mg:C of 1:1:2 in molar ratio) at 8 kbar and 420 °C using
264 Perple_X software (version 6.7.4; [Connolly, 2005](#)) and the internally consistent

265 thermodynamic database of [Holland and Powell \(1998\)](#) revised in 2004
266 (hp04ver.dat). The P – T conditions were chosen based on the onset of retrograde
267 serpentinization in the Tianshan ([Li et al., 2007, 2010](#)). Thermodynamic
268 parameters of phases belonging to the system are provided in [Supplementary](#)
269 [Table S1](#), most of which are available from literatures ([Robie and Hemingway,](#)
270 [1995; Holland and Powell, 1998; Fukui et al., 2003](#)) while the thermal expansion
271 coefficient of portlandite was calculated based on the cell volume changes during
272 heating from [Xu et al. \(2007\)](#). Redox buffers of magnetite–hematite (MH),
273 fayalite–magnetite–quartz (FMQ), and iron–magnetite (IM) were calculated for
274 reference at 8 kbar and 420 °C. The thermodynamic model of H₂O was performed
275 using the Fluids routine (H–O MRK hybrid–EoS) of the `Perple_X` software,
276 which will be discussed in [Section 4.4](#).

277 To investigate the equilibrated phase assemblages of reduced ophidolomites
278 during the retrograde serpentinization, we computed P – T pseudosections for a
279 representative sample C1534 in the Ca–Fe–Mg–Si–C–O–H system. The applied
280 solid solution models and their sources are provided in [Supplementary Table S2](#).
281 The bulk-rock composition used for the pseudosections was measured by X-ray
282 fluorescence (XRF) spectrometry at the National Research Center for Geoanalysis,
283 Chinese Academy of Geological Science. The contents of major oxides and loss
284 on ignition (LOI) are listed in [Table 1](#), with the analytical uncertainties better than
285 5%. To specify C as the thermodynamic components, we further derived the
286 effective bulk-rock composition ([Table 1](#)) by integrating mineral compositions

287 and modes, in which the H₂O and CO₂ contents were calculated based on the
288 abundances of hydrous minerals and carbonates in the sample (see [Li et al., 2012](#)
289 and [Peng et al., 2020](#) for similar approaches).

290

291 **4. RESULTS**

292 **4.1. Petrography and mineral chemistry of ophidolomites**

293 The studied ophidolomites consist primarily of antigorite and dolomite,
294 while calcite, brucite, magnetite, and olivine are present as minor or accessory
295 phases. Microstructures show a replacement texture in which dolomite grows at
296 the expense of antigorite ([Fig. 2C and D](#)). In most cases, dolomite grains have
297 experienced various degrees of decomposition, resulting in the formation of
298 acicular calcite–brucite intergrowths ([Fig. 2E–G](#)). This transformation propagates
299 inside dolomite along microcracks ([Fig. 2G](#)), which, together with patches of
300 relict dolomite in calcite products ([Fig. 2H](#)), suggests the retrograde
301 decomposition postdating dolomite formation. Olivine occurs as relicts in the
302 antigorite matrix ([Fig. 3A](#)) and inclusions (in association with antigorite and
303 brucite) within magnetite ([Fig. 3B and C](#)). Magnetite grains, ranging in size from
304 one to several millimeters, commonly enclose a variety of minerals that are
305 dominated by antigorite and dolomite ([Fig. 3B](#)). In some of the magnetite-hosted
306 mineral inclusions, the replacement of dolomite by calcite and brucite are
307 observed ([Fig. 3D](#)).

308 Representative mineral compositions of the studied ophidolomites are
309 presented in [Table 2](#). Antigorite and dolomite show nearly identical X_{Mg} (= $\text{Mg}/(\text{Mg} + \text{Fe})_{\text{molar}}$) values of 0.958–0.985 and 0.955–0.991 ([Supplementary Fig. S1](#)), respectively, in agreement with the petrographically recognized dolomite
311 growth at the expense of antigorite ([Fig. 2C and D](#)). Also, the acicular brucite
312 intergrown with calcite exhibits similar X_{Mg} values of 0.963–0.992
313 ([Supplementary Fig. S1](#)), in accord with the petrographic identification of
314 dolomite transformation into calcite and brucite ([Fig. 2E–H](#)). By contrast, olivine
315 displays relatively lower X_{Mg} values of 0.932–0.933, comparable to those of
316 metamorphic olivine ($X_{\text{Mg}} = 0.91\text{--}0.93$) in associated UHP serpentinites
317 ([Supplementary Fig. S1](#); [Shen et al., 2015](#)).

319 **4.2. Petrography, Raman spectroscopy, and microthermometry of fluid** 320 **inclusions**

321 Abundant fluid inclusions, variable in both shapes (spherical, sub-spherical,
322 and tubular) and sizes (from submicron to $\sim 8\ \mu\text{m}$), are observed in dolomite in the
323 studied ophidolomites. These fluid inclusions are grouped into fluid inclusion
324 assemblages (FIAs) based on petrographic criteria ([Goldstein and Reynolds, 1994](#);
325 [Bodnar, 2003](#)), and two main types of FIAs are further distinguished at room
326 temperatures. Fluid inclusions in the pervasive Type-I FIAs contain vapor and
327 liquid phases and show weak optical contrast to dolomite ([Fig. 4A and B](#)).
328 Typically, these two-phase fluid inclusions are liquid-rich and have less variable
329 vapor to liquid ratios of about 5–15 vol% ([Fig. 4A and B](#)). Conversely, fluid

330 inclusions in Type-II FIAs commonly contain a single phase and show strong
331 optical contrast to dolomite (Fig. 4C and D). In most cases, both types of FIAs
332 form trails crosscutting grain boundaries (Fig. 4A–D), indicating their entrapment
333 later than the host dolomite. However, the cloudy appearance and fine grain sizes
334 of calcite–brucite intergrowths (Fig. 2E–H) have significantly hindered the
335 recognition of calcite-hosted fluid inclusions. Despite this, two-phase fluid
336 inclusions are observed in calcite owing to the movement of vapor bubbles inside,
337 which are mostly isolated and randomly distributed, probably reflecting fluid
338 entrapment during the growth of calcite (Fig. 4E–G and Supplementary Fig. S2A
339 and B).

340 Raman spectroscopic and microthermometric studies were conducted on the
341 fluid inclusions. In Type-I fluid inclusions, the gaseous and liquid species are rich
342 in CH₄ and H₂O, respectively, whereas the strong fluorescence interference of the
343 host carbonates sometimes impedes direct observation of the H₂O peaks (Fig. 5A
344 and B; see also Yang et al., 2018). In contrast, dolomite-hosted Type-II fluid
345 inclusions certainly contain CH₄, while H₂ was occasionally detected (Fig. 5C).
346 In rare cases, calcite and brucite were detected in only a few of dolomite-hosted
347 Type-II fluid inclusions, which, however, cannot be unequivocally considered as
348 daughter minerals (Supplementary Fig. S2C). Overall, Type-I vapor- and liquid-
349 bearing fluid inclusions show relatively consistent final ice melting temperatures
350 (T_m) of –3.6 to –1.3 °C, corresponding to salinities of 2.2–5.9 wt% NaCl (Table
351 3). Moreover, these two-phase fluid inclusions have generally comparable

352 homogenization temperatures (T_h) of 180–230 °C, pressures at homogenization
353 (P_h) of 9–27 bar, and isochore slopes (dP/dT) of 14.2–17.0 (Table 3).

354 4.3. Isotope geochemistry

355 Representative Sr isotope compositions of dolomite and calcite in the studied
356 ophidolomites are listed in Table 4. Dolomite has $^{87}\text{Sr}/^{86}\text{Sr}$ ratios of 0.70476–
357 0.70757 (average = 0.70566, $n = 50$), lower than those of Ordovician–
358 Carboniferous (lifetime of the south Tianshan paleo-ocean; Xia et al., 2014)
359 seawater ($^{87}\text{Sr}/^{86}\text{Sr} = \text{ca. } 0.7076\text{--}0.7092$; Veizer et al., 1999) but similar to those
360 of associated HP ophidolomites and their dolomite separates ($^{87}\text{Sr}/^{86}\text{Sr} = \text{ca.}$
361 0.7064–0.7075; Peng et al., 2020) (Fig. 6A). In contrast, calcite shows relatively
362 higher $^{87}\text{Sr}/^{86}\text{Sr}$ ratios of 0.70867–0.70986 (average = 0.70938, $n = 46$), which are
363 comparable to those of the seawater as well as serpentinites in the Tianshan (Peng
364 et al., 2020) (Fig. 6A).

365 Detailed C and O isotope values of dolomite, calcite, and bulk carbonate in
366 the studied ophidolomites are shown in Table 5. Dolomite and calcite have $\delta^{13}\text{C}$
367 values of +9.2‰ ~ +11.7‰ and +7.0‰ ~ +9.0‰, respectively, similar to those of
368 bulk carbonate ($\delta^{13}\text{C} = +8.6\text{‰} \sim +10.3\text{‰}$) (Fig. 6B). These C isotope values are
369 significantly higher than $\delta^{13}\text{C}$ of marine carbonates (–3‰ ~ +3‰; Hoefs, 2009)
370 and carbonate-bearing but CH₄-absent lithologies from the Tianshan (mostly ≤
371 0‰; van der Straaten et al., 2012; Collins et al., 2015; Peng et al., 2018, 2020;
372 Zhu et al., 2018) (Fig. 6B). Moreover, dolomite and calcite display $\delta^{18}\text{O}$ values of
373 +8.1‰ ~ +9.6‰ and +8.4‰ ~ +12.6‰, respectively (Fig. 6B).

374 4.4. Thermodynamic results

375 In the $f\text{O}_2$ - $f\text{H}_2$ equilibrium diagram of Fig. 7A, the stability field of dolomite,
376 shrinking with the elevated $\log f\text{H}_2$ values, extends down to $\log f\text{O}_2 = -29.1$
377 ($\Delta\text{FMQ} -2.5$, where ΔFMQ refers to the deviation of $\log f\text{O}_2$ from the FMQ buffer)
378 at $\log f\text{H}_2 < 1.4$. The boundary between dolomite and the phase assemblage of
379 calcite + brucite + CH_4 is constrained at $\log f\text{O}_2 = -27.3 \sim -20.6$ ($\Delta\text{FMQ} -0.7 \sim$
380 $+6.0$) and $\log f\text{H}_2 = 0.3 \sim 1.4$. In the H-O system, pure H_2O ($y_{\text{H}_2\text{O}} = 1$, where $y_{\text{H}_2\text{O}}$
381 is the molar fraction of H_2O in fluids) is characterized by an ideal X_{O} ($= \text{O}/(\text{O} +$
382 $\text{H})_{\text{molar}}$) of $1/3$. In the vicinity of this value, only negligible amounts of O_2 or H_2 is
383 encompassed due to the $f\text{O}_2$ - and $f\text{H}_2$ -dependent H_2O dissociation, representing
384 slightly oxidized or reduced conditions, respectively (e.g., Connolly, 1995). In
385 this study, we superposed the thermodynamically calculated model of slightly
386 reduced H_2O at $X_{\text{O}} = 0.33 \sim 1/3$ on the $f\text{O}_2$ - $f\text{H}_2$ diagram (Fig. 7A), based on the
387 inferred serpentinization-derived fluids responsible for dolomite reduction
388 (Section 5.2) and the widely distributed aqueous fluid inclusions but the
389 sporadically detected H_2 in the studied rocks (Figs. 4 and 5; Section 4.2). Although
390 the reactive reduced fluids may potentially contain small amounts of other
391 components (see below), they do not significantly affect our model calculations
392 performed in the H-O system. Firstly, the fluids are likely CO_2 -poor, because
393 fluid inclusions do not contain detectable CO_2 in the studied ophidolomites and
394 carbonate minerals are not widely distributed in surrounding rodingites formed by
395 interactions with fluids related to the retrograde serpentinization (Li et al., 2007,

396 [2010; Shen et al., 2012, 2016](#)). Alternatively, preexisting C-bearing species (e.g.,
397 CO₂) in the fluids may have been reduced into CH₄ during the serpentinization,
398 as recorded in partially serpentinized rocks in comparable metamorphic settings
399 ([Sachan et al. 2007; Vitale Brovarone et al., 2020; Boutier et al., 2021](#)). In this
400 scenario, we set C concentrations of 0.001–0.05 molal in the fluids equilibrated
401 with carbonate-undersaturated to carbonate-saturated serpentinites at the studied
402 *P–T* conditions ([Vitale Brovarone et al., 2020](#)), and the calculated mole fractions
403 of H₂O are significantly higher than those of other molecular species (e.g., CH₄,
404 CO₂, and H₂) at X_{O} close to 1/3 ([Supplementary Fig. S3](#)). Secondly, even though
405 halogens (e.g., chlorine, Cl) commonly occur in serpentinizing fluids that may
406 decrease the activity of H₂O (e.g., [Lamadrid et al., 2017, 2021](#)), CH₄-bearing
407 aqueous fluid inclusions in the studied rocks contain relatively low salinities of
408 2.2–5.9 wt% NaCl ([Table 3](#)). These salinities correspond to H₂O mole fractions
409 of ca. 0.981–0.993 in the fluids, and thus have a negligible effect on the activity
410 of H₂O (e.g., [Aranovich and Newton, 1996](#)). Thirdly, thermodynamic calculations
411 predicted very low electrolyte concentrations of ca. 0.004–0.03 molal (mainly Si,
412 Mg, and Ca) in the fluids equilibrated with the Tianshan serpentinites during
413 retrogression ([Supplementary Fig. S4](#)), indicating that these electrolytic solutes
414 cannot profoundly affect the homogeneous equilibria among the dominant
415 molecular species and thus the application of molecular fluid models ([Connolly
416 and Galvez, 2018](#)). It is therefore likely that the possible existence of dissolved
417 species (e.g., CO₂, Cl, and other electrolytes) in the reactive reduced fluids have

418 only minor effects on the calculations in our model. The $f\text{O}_2$ – $f\text{H}_2$ equilibrium
419 diagram illustrates that an infiltration of H_2O -rich fluids characterized by
420 relatively high $f\text{H}_2$ values can contribute to abiotic CH_4 formation through
421 dolomite reduction at the studied P – T conditions (Fig. 7A). For instance, at $X_{\text{O}} =$
422 0.3333323 (corresponding to $y_{\text{H}_2\text{O}} = 0.999995$ and $y_{\text{H}_2} = 0.000005$; star in Fig. 7A),
423 the H_2O -rich fluids buffered at $\log f\text{O}_2 = -26.0$ ($\Delta\text{FMQ} + 0.6$) show a $\log f\text{H}_2$ value
424 of 0.8 and equilibrate with the phase assemblage of calcite + brucite + CH_4 .

425 The calculated P – T pseudosection for the reduced ophidolomite (Sample
426 C1534) at $\log f\text{O}_2 = -26.0$ and $\log f\text{H}_2 = 0.8$ (star in Fig. 7A) suggests that the
427 observed phase assemblage of antigorite + brucite + calcite + magnetite + CH_4
428 can be predicted at 7–9 kbar and 410–430 °C (Fig. 7B). Similar results computed
429 at $\log f\text{O}_2 = -25.8$ and $\log f\text{H}_2 = 0.7$ (Supplementary Fig. S5A) indicate that
430 variable $f\text{O}_2$ and $f\text{H}_2$ of the fluids in equilibrium with calcite + brucite + CH_4 have
431 no significant effects on the P – T pseudosection. However, since the constrained
432 $\log f\text{O}_2$ and $\log f\text{H}_2$ values for these calculations depend on and vary with P – T
433 conditions, uncertainties may occur in the phase stabilities predicted at P – T
434 conditions considerably higher or lower than 7–9 kbar and 410–430 °C in Fig. 7B
435 and Supplementary Fig. S5A. Further, the P – T pseudosection was calculated for
436 the sample without $f\text{O}_2$ and $f\text{H}_2$ constraints, demonstrating that the unreduced
437 mineral assemblage of antigorite + brucite + dolomite + calcite + magnetite can
438 remain stable at the studied P – T conditions (Supplementary Fig. S5B).

439

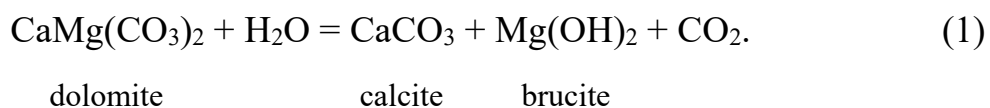
440 5. DISCUSSION

441 Ophicarbonates play a potential role in contributing to the subduction influx
442 of C (Dasgupta and Hirschmann, 2010; Alt et al., 2012, 2013) and recording the
443 mechanisms of C mobility and percolation at convergent plate boundaries
444 (Scambelluri et al., 2016; Vitale Brovarone et al., 2017; Piccoli et al., 2018;
445 Cannaò et al., 2020; Peng et al., 2020). Marine-originated ophicarbonates (mainly
446 ophicalcites) are typically characterized by Ca-carbonate matrix cementing
447 serpentinite clasts or Ca-carbonate veins filling fractured serpentinites (Bonatti et
448 al., 1974; Früh-Green et al., 2003; Schwarzenbach et al., 2013; Clerc et al., 2014;
449 Lafay et al., 2017). Subseafloor mixing zones between these pristine ophicalcites
450 and serpentinites may have served as incubators for biological communities in the
451 hydrated oceanic mantle, offering insights into deep chemolithoautotrophic life
452 (Klein et al., 2015). Moreover, HP carbonation of subduction-zone serpentinites
453 through interactions with slab-released CO₂-bearing fluids has been increasingly
454 recognized, providing implications for the distribution of subducted C
455 (Scambelluri et al., 2016; Piccoli et al., 2018; Peng et al., 2020). The Changawuzi
456 HP ophidolomites (15–25 kbar and 550–600 °C) have been studied in detail by
457 Peng et al. (2020), which are characterized by carbonate growth at the expense of
458 silicates in the host serpentinites and record interactions with CO₂-bearing fluids
459 emanating from metamafic and/or metasedimentary rocks in the subduction zone.
460 Similarly, the replacement of metamorphic antigorite by dolomite (Fig. 2C and D)
461 and their compositional inheritance (e.g., X_{Mg} values; Supplementary Fig. S1) in

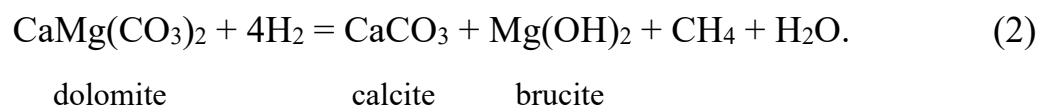
462 the studied CH₄-bearing ophidolomites point to dolomite formation through
463 interactions between CO₂-bearing fluids and serpentinites during metamorphism.
464 This is reflected by Sr isotope compositions of dolomite in these rocks
465 considerably distinct from those of seawater in the south Tianshan paleo-ocean
466 but generally similar to those of associated HP ophidolomites and their dolomite
467 separates (Fig. 6A), likely inheriting the low ⁸⁷Sr/⁸⁶Sr values of subducted
468 carbonate-bearing lithologies in the Tianshan (Peng et al., 2020). Microstructures,
469 mineral compositions, and Sr isotopic signatures of the studied CH₄-bearing
470 ophidolomites are comparable to those of HP ophidolomites in the same study
471 area (Peng et al., 2020), indicating that they likely record the consistent HP
472 carbonation of serpentinites in the subduction zone. Even though obtaining
473 precise *P–T* constraints for dolomite formation in the studied rocks is relatively
474 difficult, it may not considerably affect the following discussion with respect to
475 dolomite reduction and abiotic CH₄ generation in the subduction zone.

476 **5.1. Abiotic CH₄ generation through dolomite reduction**

477 Intergrowths of calcite and brucite in natural rocks (Fig. 2E–H) are relatively
478 hard to be preserved because these fine and soluble minerals are easily removed
479 by an abundance of circulating fluids (Berg, 1986). The retrograde decomposition
480 of dolomite into calcite–brucite intergrowths was observed in mantle wedge
481 ultramafic rocks and interpreted as Reaction (1), which occurred by infiltration of
482 H₂O at oxidized conditions (Förster et al., 2017; Consuma et al., 2020):



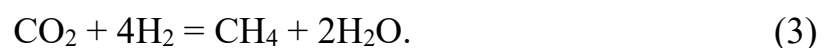
483 In this study, by contrast, the pervasive occurrence of $\text{CH}_4 \pm \text{H}_2\text{O} \pm \text{H}_2$ in
 484 dolomite- and calcite-hosted fluid inclusions (Figs. 4 and 5) likely suggests
 485 reduced aqueous fluids responsible for the decomposition of dolomite.
 486 Nevertheless, the limited distribution of H_2 in the fluid inclusions (Section 4.2) is
 487 probably indicative of its minor proportion in the reactive aqueous fluids, or,
 488 alternatively, ascribed to several other potential processes (see below).
 489 Thermodynamic calculations further demonstrate that an infiltration of H_2O -rich
 490 fluids, characterized by a relatively high $\log f\text{H}_2$ value of 0.8 but containing a low
 491 H_2 molar fraction of 0.000005 (star in Fig. 7A), can result in the transformation
 492 of dolomite into the phase assemblage of calcite + brucite + CH_4 , which is
 493 expressed by the $f\text{H}_2$ -dependent Reaction (2):



494 This CH_4 -generating reaction is endorsed by the notably high $\delta^{13}\text{C}$ values of
 495 carbonates in the studied rocks (Fig. 6B). The positive shift in $\delta^{13}\text{C}$ is exactly
 496 opposite to the typical C isotopic trend related to decarbonation reactions and/or
 497 carbonate–organic matter re-equilibrations as also recorded in the Tianshan (Fig.
 498 6B; Collins et al., 2015; Zhu et al., 2018). Similar high $\delta^{13}\text{C}$ values were
 499 interpreted as evidence for carbonate reduction forming graphite (Galvez et al.,
 500 2013b) or abiotic CH_4 (Vitale Brovarone et al., 2017) in comparable metamorphic
 501 settings. Based on $\delta^{13}\text{C}$ of calcite (Table 5) and the equilibrium fractionation

502 factor between calcite and CH₄ ($\ln\alpha(\text{CaCO}_3\text{--CH}_4) = +15.0\text{‰} \sim +16.0\text{‰}$ at 410–
503 430 °C; [Bottinga, 1969](#)), we calculated C isotope compositions of CH₄ ranging
504 from –9.0‰ to –6.0‰. These values fit the range of C isotope compositions of
505 abiotic CH₄ from worldwide occurrences, which display $\delta^{13}\text{C}$ values typically
506 higher than ca. –25‰ (e.g., [Ueno et al., 2006](#); [Etiope et al., 2011](#)). Considering
507 that dolomite in the studied ophidolomites is likely related to the HP carbonation
508 of serpentinites (see above), its heavy $\delta^{13}\text{C}$ values relative to those in associated
509 HP ophidolomites ([Fig. 6B](#)) are probably attributed to an additional reduction
510 process of dolomite other than Reaction (2). In this process, dolomite may have
511 been decomposed into CH₄ together with aqueous species such as Ca²⁺ and Mg²⁺,
512 which represents the reduction of dissolved C-bearing species (e.g., CO₃²⁻, HCO₃⁻,
513 and/or CO_{2,aq}) of dolomite (see [Frezzotti et al., 2011](#); [Ague and Nicolescu, 2014](#);
514 [and Facq et al., 2014](#) for carbonate dissolution in subduction zones). In addition
515 to the potential dissolution-induced dolomite reduction, other processes resulting
516 in C isotopic enrichment of the residual dolomite may also be possible.

517 It is apparent that Reaction (2) essentially reflects a H₂O-triggered
518 decarbonation process of dolomite (Reaction (1)) coupled with a coinstantaneous
519 $f\text{H}_2$ -dependent reduction process of CO₂ (Reaction (3)):



520 In this study, however, the decarbonation of dolomite is not spontaneous in
521 reduced environments and thus seems unlikely to proceed independently prior to
522 the reduction of CO₂ (see below). Firstly, the fluid inclusions do not contain

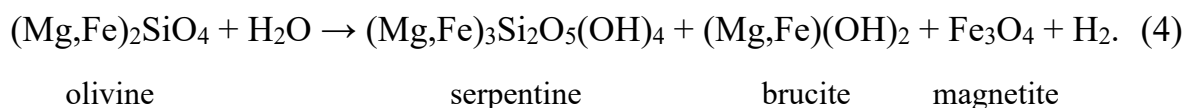
523 detectable CO₂ as the intermediate product, in which CH₄ occurs as the dominant
524 C-bearing species instead. The isolated and randomly distributed CH₄-bearing
525 fluid inclusions in calcite may provide further evidence for the simultaneous
526 production of CH₄ and calcite through dolomite decomposition (Fig. 4E–G and
527 [Supplementary Fig. S2A](#) and B). Secondly, the retrograde serpentinization
528 responsible for abiogenic CH₄ formation ([Section 5.2](#)) started at 7–9 kbar and 410–
529 430 °C and propagated to lower *P–T* conditions (e.g., 2–10 kbar and 250–350 °C;
530 [Li et al., 2007, 2010](#)), indicating that dolomite decarbonation, if it exists, should
531 take place at oxidized conditions prior to the retrograde serpentinization. In this
532 scenario (i.e., *P* > 7–9 kbar and *T* > 410–430 °C), aragonite is likely to replace
533 calcite as the dominant Ca-carbonate products (cf. the calcite–aragonite transition
534 in [Fig. 8](#); [Johannes and Puhan, 1971](#)), inconsistent with the observed calcite–
535 brucite intergrowths in the studied ophidolomites ([Fig. 2E–H](#)). Thirdly, the
536 elevated C isotope values of calcite, contrary to the negative shift of δ¹³C derived
537 from carbonate decarbonation ([Fig. 6B](#)), provide geochemical constraints on the
538 equilibrium between calcite and CH₄ in the studied ophidolomites (see above).
539 An alternative explanation may exist for these results that dolomite has recorded
540 ¹³C enrichment (e.g., through dissolution-induced reduction; see above) prior to
541 the decoupled dolomite decarbonation and CO₂ reduction processes, but such
542 cyclic redox transformations (i.e., reduction–oxidation–reduction) are not
543 reported in the study area ([Li et al., 2007, 2010](#)).

544 Although our model calculations demonstrate that H₂O-rich fluids at
545 relatively high f_{H_2} (e.g., $y_{\text{H}_2\text{O}} = 0.999995$ at $\log f_{\text{H}_2} = 0.8$; star in Fig. 7A) can
546 create favorable conditions for dolomite reduction and abiotic CH₄ generation, the
547 possibility of carbonate methanation by H₂-rich fluids cannot be excluded. The
548 latter case has been reported in subducted ophicalcites in the Western Alps,
549 recording a H₂-induced calcite methanation process in which the equilibrated
550 fluids are characterized by dominant CH₄ while $y_{\text{H}_2\text{O}} = y_{\text{H}_2}$ at $X_{\text{O}} < 0.03$ at 7 kbar
551 and 350 °C (Vitale Brovarone et al., 2017). In this scenario, H₂ is not pervasively
552 detected by Raman spectroscopy in fluid inclusions in the studied rocks (Figs. 4
553 and 5; Section 4.2) probably because it has been largely consumed by carbonate
554 reduction to CH₄ (e.g., Grozeva et al., 2020). Alternatively, H₂ could potentially
555 occur in the fluid inclusions but the Raman peaks have been severely obscured by
556 the strong fluorescence of the host carbonates (Fig. 5). Overall, there is no
557 petrographic evidence for post-entrapment re-equilibrations of the fluid inclusions
558 (e.g., stretching, leakage, and decrepitation), as supported by their relatively
559 consistent vapor to liquid ratios (Fig. 4A and B; Section 4.2), homogenization
560 temperatures (Table 3), and Raman peak positions of gaseous CH₄
561 (Supplementary Table S3) within an individual FIA (e.g., Bodnar, 2003; Lin et
562 al., 2007). Concentrations of molecular species as a function of X_{O} in the graphite-
563 buffered COH system calculated at 7 kbar and 350 °C (Vitale Brovarone et al.,
564 2017; see Supplementary Fig. S6 for similar calculations at the studied P - T
565 conditions) illustrate that mole fractions of H₂O in the fluids, relative to CH₄ and

566 H₂, progressively increase with X_O (until at X_O = 1/3). Such calculations suggest
567 that determination of proportions of these species in the equilibrated fluids may
568 provide important insights into the reduced nature of the reactive fluids (i.e., H₂O-
569 rich fluids at relatively high fH₂ vs. H₂-rich fluids).

570 **5.2. Reduced fluid source(s) and fluid inclusion entrapment**

571 The reactive reduced fluids are likely associated with retrograde
572 serpentinization in the Tianshan, during which the observed phase assemblage in
573 the studied rocks can remain stable (Fig. 7B and Supplementary Fig. S5). Even
574 though fluid source(s) responsible for the retrograde serpentinization is(are)
575 largely unresolved (Li et al., 2007, 2010), the preservation of Sr and O isotopic
576 signatures of seawater in the Tianshan serpentinites (Scicchitano et al., 2018; Peng
577 et al., 2020) suggests that these rocks may record interactions with fluids
578 migrating upward from serpentinite dehydration at greater depths (see also
579 Angiboust et al., 2014 and Piccoli et al., 2018). Serpentinization of olivine
580 provides a potential source for H₂, together with the concomitant formation of
581 magnetite (Reaction (4); e.g., McCollom and Bach, 2009; Klein et al., 2013, 2020).



582 Although the possibility for serpentinization of olivine to produce H₂ at high
583 temperatures (400–600 °C) has been questioned (Evans, 2010), recent studies
584 show that magnetite formation and H₂ generation through HP serpentinization
585 may be common under several subduction zone conditions (Vitale Brovarone et

586 [al., 2020; Boutier et al., 2021](#)). Thus, olivine relicts in the antigorite matrix ([Fig.](#)
587 [3A](#)), as well as the occurrence of olivine (in association with antigorite and brucite)
588 and dolomite decomposition within magnetite ([Fig. 3B–D](#)), suggest that the
589 studied ophidolomites may have acted as a possible H₂ source for the reduction
590 process. Alternatively, the reduced fluids may be externally derived from the
591 rehydration of surrounding serpentinites, which contain ~25 vol% metamorphic
592 olivine ([Shen et al., 2015](#)). Moreover, the elevated ⁸⁷Sr/⁸⁶Sr ratios of calcite,
593 decoupled from dolomite but in general agreement with the Tianshan serpentinites
594 that have largely inherited Sr isotope values of the seawater ([Fig. 6A; Peng et al.,](#)
595 [2020](#)), likely reflect Sr isotope exchange with the serpentinizing fluids during
596 dolomite reduction.

597 In the studied rocks, a majority of dolomite-hosted fluid inclusions form
598 trails crosscutting grain boundaries ([Fig. 4A–D](#)), indicating that they were trapped
599 along fractures of dolomite and preserved through subsequent healing of these
600 fractures. The relative timing of fluid entrapment can be obtained by fluid
601 inclusion isochores intersecting the retrograde path of the Chinese southwestern
602 Tianshan ([Tan et al., 2017](#)), which constrained *P–T* conditions of about 1–3 kbar
603 and 250–350 °C ([Fig. 8](#)). The *P–T* constraints, lower than 7–9 kbar and 410–430
604 °C, suggest that entrapment of the fluid inclusions postdates the onset of dolomite
605 reduction ([Fig. 8](#)). Based on the localized alteration of dolomite ([Fig. 2](#)), we infer
606 that the reactive reduced fluids may be limited and have been largely consumed
607 by dolomite after the reduction started, leading to the stability of relict reactants

608 until the fractures were generated to provide fluid pathways and subsequently
609 healed to preserve the fluid inclusions. This is in agreement with our petrographic
610 observations that dolomite-hosted fluid inclusions are nearly devoid of calcite and
611 brucite daughter minerals representative of dolomite reduction within the
612 inclusions (Section 4.2). Given that the retrograde serpentinization responsible for
613 dolomite reduction could propagate to relatively lower P - T conditions (e.g., 2–10
614 kbar and 250–350 °C; Li et al., 2007, 2010), the possibility may exist that the
615 timing of fluid inclusion trapping is slightly later than or close to that of abiotic
616 CH_4 formation. Under this circumstance, the reduction process of dolomite
617 probably came to a halt due to the exhaustion of the reactive reduced fluids (see
618 above), closely followed by fluid entrapment along the fractures. Note that this
619 possibility depends primarily on P - T conditions for the propagation of the
620 retrograde serpentinization, which, however, remain uncertain despite the
621 calculations by Li et al. (2007, 2010) based on a few reactions observed in
622 serpentinites and associated rodingites. Uncertainties may mainly derive from the
623 controversial P - T conditions for the transformation of chrysotile into antigorite
624 (Evans et al., 1976; Scambelluri et al., 2004; Li et al., 2007, 2010) and the
625 ignorance of several potential reactions (e.g., the lizardite to antigorite transition;
626 Guillot et al., 2015) in rocks for the constraints (Fig. 8).

627 **5.3. Implications for C mobility in subduction zones**

628 Laboratory studies demonstrated that carbonate aqueous reduction at $f\text{O}_2$ far
629 below the FMQ buffer (e.g., the IM or iron-wüstite (IW) buffer) under HP

630 conditions is a potential pathway for significant production of abiotic CH₄ in
631 subduction zones (Lazar et al., 2014; Mukhina et al., 2017). Moreover, field-based
632 investigations constrained a relatively wide range of log f_{O_2} values for HP abiotic
633 formation of CH₄ via carbonate reduction in opicalcites from the Western Alps
634 (ΔFMQ $-6.0 \sim -3.0$ at 1 GPa and 400 °C; Vitale Brovarone et al., 2017) and in
635 carbonated eclogites from the Tianshan (ΔFMQ -2.5 at 2.5 GPa and 550 °C; Tao
636 et al., 2018a). In the present study, thermodynamic simulations suggest that
637 abiotic CH₄ generation through dolomite aqueous reduction can occur at f_{O_2}
638 slightly lower than or even close to the FMQ buffer (Fig. 7A). The stability of
639 CH₄-bearing fluids at FMQ conditions is reflected by a three-dimensional P - T -
640 log f_{O_2} diagram calculated for graphite/diamond-saturated COH fluids (Tumiati
641 and Malaspina, 2019), displaying that the FMQ surface is below the maximum
642 H₂O activity surface where CH₄ is the dominant C-bearing species under the
643 studied P - T conditions. Furthermore, experiments conducted on HP aqueous
644 reduction of organic matter demonstrated that CH₄-bearing fluids in equilibrium
645 with graphite can stabilize at f_{O_2} approaching the FMQ buffer (i.e., the Co-CoO
646 or Ni-NiO buffer at 2.5 GPa and 600–700 °C; Li, 2017). In the studied samples,
647 however, graphite was sporadically detected in the cloudy calcite-brucite
648 intergrowths (Supplementary Fig. S7), which may be attributed to the high f_{H_2}
649 conditions (see below).

650 Graphite has been observed in several CH₄-absent (Malvoisin et al., 2012;
651 Galvez et al., 2013a, b; Zhu et al., 2020) or CH₄-bearing (Vitale Brovarone et al.,

652 2017, 2020; Tao et al., 2018a) lithologies in subduction zones, formed by
653 carbonate anhydrous graphitization or precipitating from the reduced COH fluids.
654 Compared with carbonate minerals (e.g., Kelemen and Manning, 2015), graphite
655 represents a relatively stable phase that may transfer subducted C into the deep
656 Earth (Galvez et al., 2013a; Duncan and Dasgupta, 2017; Eguchi et al., 2020),
657 while recent studies suggest that graphite could be partly dissolved in subduction-
658 zone fluids (Tumiati et al., 2017, 2020 and references therein). In our study,
659 however, the widespread occurrence of CH₄ compared to graphite illustrates that
660 the equilibrium between graphite and CH₄ may be largely controlled by fH_2 (Fig.
661 7A), implying that an increase in fH_2 would contribute to the transformation of
662 graphite into CH₄ at convergent plate boundaries. This is in accord with the
663 microstructure-based recognition of an additional abiotic CH₄-forming event in
664 reduced ophicalcites from the Western Alps, attributed to H₂-induced reduction
665 of the newly formed graphite during ascent of the slab (Vitale Brovarone et al.,
666 2017). Moreover, experiments performed on the hydrogenation of graphite at high
667 P – T conditions (5.0–5.5 GPa and >1500 °C) yielded considerable CH₄, indicating
668 that fH_2 may play an important role in governing abiotic CH₄ genesis in deep
669 subduction zones (Sharma et al., 2009). Indeed, graphite has a very low content
670 or nearly absent in several CH₄–H₂-bearing serpentinites in subduction zones
671 (Peretti et al., 1992; Vitale Brovarone et al., 2020), in agreement with the CH₄–
672 H₂–H₂O equilibrated region below the graphite saturation curve predicted by the
673 isobaric–isothermal C–O–H diagram (e.g., Holloway, 1984).

674 While the reduction in our study happened during exhumation of the slab,
675 the proposed P – T estimates are similar to those of carbonate reduction during
676 shallow subduction in comparable metamorphic settings (Malvoisin et al., 2012;
677 Galvez et al., 2013a, b; Vitale Brovarone et al., 2017; Giuntoli et al., 2020), which
678 are in general accord with the prograde P – T paths of subduction zones predicted
679 by thermal models (Syracuse et al., 2010) and metamorphic rocks (Penniston-
680 Dorland et al., 2015) (Fig. 9A). Thus, the reduction process of dolomite described
681 here may have implications for subducted C mobility. Laboratory experiments
682 and field observations provide evidence for dolomite formation through mineral
683 carbonation in subseafloor serpentinization systems (Grozeva et al., 2017),
684 suggesting that subduction of these hydrothermally altered oceanic rocks
685 represents a potential dolomite source in downgoing slabs. Indeed, dolomite,
686 despite its variable contents (ca. 5–50 vol%), is not uncommon in several slab-
687 and mantle wedge-forming lithologies including metaultramafic, metamafic, and
688 metasedimentary rocks (e.g., Li et al., 2012, 2014; Tao et al., 2014, 2018b; Falk
689 and Kelemen, 2015; Zhu et al., 2018). Furthermore, mounting field evidence, as
690 well as thermodynamic modelling, suggests that serpentinization of ultramafic
691 rocks can happen at relatively shallow depths (ca. 20–30 km) in subducted slabs,
692 or even up to ca. 70–80 km (Li et al., 2007, 2010; Vitale Brovarone et al., 2017,
693 2020; Lazar, 2020). Therefore, an infiltration of these serpentinization-derived
694 reduced fluids would be conducive to dolomite reduction and abiotic CH₄
695 generation during shallow subduction, which may represent a feasible mechanism

696 for the mobility of subducted C (Fig. 9B). Moreover, release of such deep-sourced
697 reduced fluids might support the hypothesis that subduction zones potentially
698 provide energy to sustain subsurface chemosynthetic microbial life at habitable
699 temperatures in the overlying forearc (e.g., Curtis et al., 2013; Plümper et al., 2017;
700 Fryer et al., 2020; Lazar, 2020; Vitale Brovarone et al., 2020; Wheat et al., 2020).
701 However, uncertainties remain regarding the implications presented here,
702 particularly under circumstances where the scale and extent of dolomite reduction
703 are insufficiently quantified.

704

705 6. CONCLUSIONS

706 Reduction of ophidolomites in the Chinese southwestern Tianshan HP–UHP
707 metamorphic belt provides new insights into abiogenic CH₄ generation in subduction
708 zones. Petrological characteristics, Raman spectroscopic and microthermometric
709 data of fluid inclusions, Sr and C isotope compositions, and thermodynamic
710 results demonstrate dolomite reduction into the phase assemblage of calcite +
711 brucite + CH₄, likely related to retrograde serpentinization starting at 7–9 kbar
712 and 410–430 °C in the subduction zone. The onset of dolomite reduction is prior
713 to fluid entrapment that happened at about 1–3 kbar and 250–350 °C, leading to
714 the widespread distribution of secondary fluid inclusions along healed fractures
715 of dolomite. Model calculations suggest that an infiltration of H₂O-rich fluids at
716 relatively high f_{H_2} (e.g., $y_{\text{H}_2\text{O}} = 0.999995$ at $\log f_{\text{H}_2} = 0.8$) can contribute to this
717 reduction process, but the possibility of carbonate methanation by H₂-rich fluids

718 cannot be excluded. The abundant CH₄-bearing fluid inclusions in these rocks
719 indicate that fH_2 probably plays an important role in regulating the speciation of
720 subducted C, implying that an increase in fH_2 may accelerate abiotic formation of
721 CH₄ through dolomite reduction at convergent plate boundaries. Thus, alteration
722 of dolomite-bearing lithologies represents a potential mechanism for abiotic
723 synthesis of CH₄ in subduction zones, which may have implications for the
724 mobility of subducted C.

725

726 **ACKNOWLEDGEMENTS**

727 This work was funded by the National Key Research and Development
728 Program of China (No. 2019YFA0708501), the National Natural Science
729 Foundation of China (No. 41520104004), and the Scientific Research Foundation
730 of Pilot National Laboratory for Marine Science and Technology (Qingdao) (No.
731 JCZX202011). Simone Tumiati acknowledges support from the Italian program
732 MIUR PRIN (No. 2017ZE49E7_002). Alberto Vitale Brovarone was supported
733 by the ERC CoG “DeepSeep” (No. 864045), an ANR T-ERC grant (No. LS
734 171301), and a MIUR Levi Montalcini grant; by the Deep Carbon Observatory
735 (DCO) Deep Energy community; and by the Richard Lounsbery foundation.
736 Discussions with James Connolly, Thomas Bader, Wen Zhang, Yueheng Yang,
737 Enrico Cannà, Ryosuke Oyanagi, Xiaoxia Li, Xia Zhang, and Shujie Wang are
738 highly appreciated. We thank Yang Wang and Zhicheng Liu for their help during
739 fieldwork, and Hongrui Ding, Liangliang Huang, Hongwei Li, Xiangtian Jin, Nan

740 Li, Xiaoli Li, and Jiangqing Liu for their patient assistance during sample analyses.
741 The authors are grateful to anonymous reviewers (three for a very early draft and
742 three for a more recent draft) for their detailed and constructive comments and to
743 Frieder Klein (Associate Editor) for his careful editorial handling and helpful
744 suggestions.

745

746 **APPENDIX A. SUPPLEMENTARY MATERIAL**

747 Supplementary data to this article can be found online at <https://doi.org/XXXX>.

748

749 **RESEARCH DATA**

750 All research data used in this study are included in tables and the appendix file.

751

752 **REFERENCES**

- 753 Ague J. J. and Nicolescu S. (2014) Carbon dioxide released from subduction
754 zones by fluid-mediated reactions. *Nat. Geosci.* **7**, 355–360.
- 755 Alt J. C., Garrido C. J., Shanks W. C., Turchyn A., Padrón-Navarta J. A., López
756 Sánchez-Vizcaíno V., Gómez-Pugnaire M. T. and Marchesi C. (2012)
757 Recycling of water, carbon, and sulfur during subduction of serpentinites: a
758 stable isotope study of Cerro del Almirez, Spain. *Earth Planet. Sci. Lett.* **327–**
759 **328**, 50–60.
- 760 Alt J. C., Schwarzenbach E. M., Früh-Green G. L., Shanks W. C., Bernasconi S.
761 M., Garrido C. J., Crispini L., Gaggero L., Padrón-Navarta J. A. and Marchesi
762 C. (2013) The role of serpentinites in cycling of carbon and sulfur: seafloor
763 serpentinitization and subduction metamorphism. *Lithos* **178**, 40–54.

- 764 Angiboust S., Pettke T., De Hoog J. C. M., Caron B. and Oncken O. (2014)
765 Channelized fluid flow and eclogite-facies metasomatism along the
766 subduction shear zone. *J. Petrol.* **55**, 883–916.
- 767 Arai S., Ishimaru S. and Mizukami T. (2012) Methane and propane micro-
768 inclusions in olivine in titanoclinohumite-bearing dunites from the Sanbagawa
769 high-P metamorphic belt, Japan: Hydrocarbon activity in a subduction zone
770 and Ti mobility. *Earth Planet. Sci. Lett.* **353**, 1–11.
- 771 Aranovich L. Y. and Newton R. C. (1996) H₂O activity in concentrated NaCl
772 solutions at high pressures and temperatures measured by the brucite–
773 periclase equilibrium. *Contrib. Mineral. Petrol.* **125**, 200–212.
- 774 Berg G. W. (1986) Evidence for carbonate in the mantle. *Nature* **324**, 50–51.
- 775 Bodnar R. J. (2003) Reequilibration of fluid inclusions. In *Fluid Inclusions:*
776 *Analysis and Interpretation* (eds. I. Samson, A. Anderson and D. Marshall).
777 Mineral Association of Canada, Short Course 32. pp. 213–230.
- 778 Bonatti E., Emiliani C., Ferrera G., Honnorez J. and Rydell H. (1974) Ultramafic-
779 carbonate breccias from the equatorial Mid Atlantic Ridge. *Mar. Geol.* **16**,
780 83–102.
- 781 Bottinga Y. (1969) Calculated fractionation factors for carbon and hydrogen
782 isotope exchange in the system calcite–carbon dioxide–graphite–methane–
783 hydrogen–water vapor. *Geochim. Cosmochim. Acta* **33**, 49–64.
- 784 Boutier A., Vitale Brovarone A., Martinez I., Sissmann O. and Mana S. (2021)
785 High-pressure serpentinization and abiotic methane formation in
786 metaperidotite from the Appalachian subduction, northern Vermont. *Lithos*
787 **396–397**, 106190.
- 788 Cannà E., Scambelluri M., Bebout G. E., Agostini S., Pettke T., Godard M. and
789 Crispini L. (2020) Ophicarbonates evolution from seafloor to subduction and
790 implications for deep-Earth C cycling. *Chem. Geol.* **546**, 119626.

- 791 Charlou J. L., Donval J. P., Fouquet Y., Jean-Baptiste P. and Holm N. (2002)
792 Geochemistry of high H₂ and CH₄ vent fluids issuing from ultramafic rocks at
793 the Rainbow hydrothermal field (36°14'N, MAR). *Chem. Geol.* **191**, 345–359.
- 794 Charlou J. L., Donval J. P., Konn C., Ondréas H., Fouquet Y., Jean-Baptiste P.
795 and Fourré E. (2010) High production and fluxes of H₂ and CH₄ and evidence
796 of abiotic hydrocarbon synthesis by serpentinization in ultramafic-hosted
797 hydrothermal systems on the Mid-Atlantic Ridge. In *Diversity of*
798 *Hydrothermal Systems on Slow Spreading Ocean Ridges* (eds. P. A. Rona, C.
799 W. Devey, J. Dymont and B. J. Murton). American Geophysical Union,
800 Washington, DC. pp. 265–296.
- 801 Clerc C., Boulvais P., Lagabrielle Y. and de Saint Blanquat M. (2014)
802 Ophicalcites from the northern Pyrenean belt: a field, petrographic and stable
803 isotope study. *Int. J. Earth Sci.* **103**, 141–163.
- 804 Collins N. C., Bebout G. E., Angiboust S., Agard P., Scambelluri M., Crispini L.
805 and John T. (2015) Subduction zone metamorphic pathway for deep carbon
806 cycling: II. Evidence from HP/UHP metabasaltic rocks and ophicarbonates.
807 *Chem. Geol.* **412**, 132–150.
- 808 Connolly J. A. D. (1995) Phase diagram methods for graphitic rocks and
809 application to the system C–O–H–FeO–TiO₂–SiO₂. *Contrib. Mineral. Petrol.*
810 **119**, 94–116.
- 811 Connolly J. A. D. (2005) Computation of phase equilibria by linear programming:
812 A tool for geodynamic modeling and its application to subduction zone
813 decarbonation. *Earth Planet. Sci. Lett.* **236**, 524–541.
- 814 Connolly J. A. D. and Galvez M. E. (2018) Electrolytic fluid speciation by Gibbs
815 energy minimization and implications for subduction zone mass transfer.
816 *Earth Planet. Sci. Lett.* **501**, 90–102.
- 817 Consuma G., Braga R., Giovanardi T., Bersani D., Konzett J., Lugli F.,
818 Mazzucchelli M. and Tropper P. (2020) *In situ* Sr isotope analysis of mantle

819 carbonates: Constraints on the evolution and sources of metasomatic carbon-
820 bearing fluids in a paleo-collisional setting. *Lithos* **354–355**, 105334.

821 Curtis A. C., Wheat C. G., Fryer P. and Moyer C. L. (2013) Mariana forearc
822 serpentinite mud volcanoes harbor novel communities of extremophilic
823 *Archaea*. *Geomicrobiol. J.* **30**, 430–441.

824 Dasgupta R. and Hirschmann M. M. (2010) The deep carbon cycle and melting
825 in Earth's interior. *Earth Planet. Sci. Lett.* **298**, 1–13.

826 Duncan M. S. and Dasgupta R. (2017) Rise of Earth's atmospheric oxygen
827 controlled by efficient subduction of organic carbon. *Nat. Geosci.* **10**, 387–
828 392.

829 Eguchi J., Seales J. and Dasgupta R. (2020) Great Oxidation and Lomagundi
830 events linked by deep cycling and enhanced degassing of carbon. *Nat. Geosci.*
831 **13**, 71–76.

832 Etiope G. and Schoell M. (2014) Abiotic gas: Atypical, but not rare. *Elements* **10**,
833 291–296.

834 Etiope G. and Sherwood Lollar B. (2013) Abiotic Methane on Earth. *Rev.*
835 *Geophys.* **51**, 276–299.

836 Etiope G., Schoell M. and Hosgörmez H. (2011) Abiotic methane flux from the
837 Chimaera seep and Tekirova ophiolites (Turkey): Understanding gas
838 exhalation from low temperature serpentinization and implications for Mars.
839 *Earth Planet. Sci. Lett.* **310**, 96–104.

840 Evans B. W. (2010) Lizardite versus antigorite serpentinite: Magnetite, hydrogen,
841 and life(?). *Geology* **38**, 879–882.

842 Evans K. A. (2012) The redox budget of subduction zones. *Earth Sci. Rev.* **113**,
843 11–32.

844 Evans B. W., Johannes W., Oterdoom H. and Trommsdorff V. (1976) Stability of
845 chrysotile and antigorite in the serpentine multisystem. *Schweiz. Mineral.*
846 *Petrogr. Mitt.* **56**, 79–93.

- 847 Facq S., Daniel I., Montagnac G., Cardon H. and Sverjensky D. A. (2014) *In situ*
848 Raman study and thermodynamic model of aqueous carbonate speciation in
849 equilibrium with aragonite under subduction zone conditions. *Geochim.*
850 *Cosmochim. Acta* **132**, 375–390.
- 851 Falk E. S. and Kelemen P. B. (2015) Geochemistry and petrology of listvenite in
852 the Samail ophiolite, Sultanate of Oman: Complete carbonation of peridotite
853 during ophiolite emplacement. *Geochim. Cosmochim. Acta* **160**, 70–90.
- 854 Förster B., Braga R., Aulbach S., Lo Pò D., Bargossi G. M. and Mair V. (2017)
855 A petrographic study of carbonate phases in the Ulten Zone ultramafic rocks:
856 Insights into carbonation in the mantle wedge and exhumation-related
857 decarbonation. *Ophioliti* **42**, 105–127.
- 858 Frezzotti M. L., Selverstone J., Sharp Z. D. and Compagnoni R. (2011) Carbonate
859 dissolution during subduction revealed by diamond-bearing rocks from the
860 Alps. *Nat. Geosci.* **4**, 703–706.
- 861 Früh-Green G. L., Kelley D. S., Bernasconi S. M., Karson J. A., Ludwig K. A.,
862 Butterfield D. A., Boschi C. and Proskurowski G. (2003) 30000 years of
863 hydrothermal activity at the Lost City vent field. *Nature* **301**, 495–498.
- 864 Fryer P., Wheat C. G., Williams T., Kelley C., Johnson K., Ryan J., Kurz W.,
865 Shervais J., Albers E., Bekins B., Debret B., Deng J., Dong Y., Eickenbusch
866 P., Frery E., Ichiyama Y., Johnston R., Kevorkian R., Magalhaes V.,
867 Mantovanelli S., Menapace W., Menzies C., Michibayashi K., Moyer C.,
868 Mullane K., Park J.-W., Price R., Sissmann O., Suzuki S., Takai K., Walter
869 B., Zhang R., Amon D., Glickson D. and Pomponi S. (2020) Mariana
870 serpentinite mud volcanism exhumes subducted seamount materials:
871 implications for the origin of life. *Phil. Trans. R. Soc. A* **378**, 20180425.
- 872 Fukui H., Ohtaka O., Fujisawa T., Kunisada T., Suzuki T. and Kikegawa T. (2003)
873 Thermo-elastic property of Ca(OH)₂ portlandite. *High Pressure Res.* **23**, 55–
874 61.

875 Galvez M. E. and Pubellier M. (2019) How do subduction zones regulate the
876 carbon cycle? In *Deep carbon: Past to Present* (eds. B. N. Orcutt, I. Daniel
877 and R. Dasgupta). Cambridge University Press, Cambridge. pp. 276–312.

878 Galvez M. E., Beyssac O., Martinez I., Benzerara K., Chaduteau C., Malvoisin B.
879 and Malavieille J. (2013a) Graphite formation by carbonate reduction during
880 subduction. *Nat. Geosci.* **6**, 473–477.

881 Galvez M. E., Martinez I., Beyssac O., Benzerara K., Agrinier P. and Assayag N.
882 (2013b) Metasomatism and graphite formation at a lithological interface in
883 Malaspina (Alpine Corsica, France). *Contrib. Mineral. Petrol.* **166**, 1687–
884 1708.

885 Giuntoli F., Vitale Brovarone A. and Menegon L. (2020) Feedback between high-
886 pressure genesis of abiotic methane and strain localization in subducted
887 carbonate rocks. *Sci. Rep.* **10**, 9848.

888 Goldstein R. H. and Reynolds T. J. (1994) *Systematics of fluid inclusions in*
889 *diagenetic minerals*. SEPM (Society for Sedimentary Geology) Short Course
890 31, Tulsa.

891 Grozeva N. G., Klein F., Seewald J. S. and Sylva S. P. (2017) Experimental study
892 of carbonate formation in oceanic peridotite. *Geochim. Cosmochim. Acta* **199**,
893 264–286.

894 Grozeva N. G., Klein F., Seewald J. S. and Sylva S. P. (2020) Chemical and
895 isotopic analyses of hydrocarbon-bearing fluid inclusions in olivine-rich rocks.
896 *Phil. Trans. R. Soc. A* **378**, 20180431.

897 Guillot S., Schwartz S., Reynard B., Agard P. and Prigent C. (2015) Tectonic
898 significance of serpentinites. *Tectonophysics* **646**, 1–19.

899 Hayes J. M. and Waldbauer J. R. (2006) The carbon cycle and associated redox
900 processes through time. *Phil. Trans. R. Soc. B* **361**, 931–950.

901 Hoefs J. (2009) *Stable Isotope Geochemistry, 6th ed.* Springer-Verlag, Berlin
902 Heidelberg.

903 Holland T. J. B. and Powell R. (1998) An internally consistent thermodynamic
904 data set for phases of petrological interest. *J. Metamorph. Geol.* **16**, 309–343.

905 Holloway J. R. (1984) Graphite–CH₄–H₂O–CO₂ equilibria at low-grade
906 metamorphic conditions. *Geology* **12**, 455–458.

907 Hu Z., Liu Y., Gao S., Xiao S., Zhao L., Günther D., Li M., Zhang W. and Zong
908 K. (2012) A “wire” signal smoothing device for laser ablation inductively
909 coupled plasma mass spectrometry analysis. *Spectrochim. Acta B* **78**, 50–57.

910 Hu H., Vitale Brovarone A., Zhang L., Piccoli F., Peng W. and Shen T. (2021)
911 Retrograde carbon sequestration in orogenic complexes: A case study from
912 the Chinese southwestern Tianshan. *Lithos* **392–393**, 106151.

913 Huang F., Daniel I., Cardon H., Montagnac G. and Sverjensky D. A. (2017)
914 Immiscible hydrocarbon fluids in the deep carbon cycle. *Nat. Commun.* **8**,
915 15798.

916 Jaeckel K., Bebout G. E. and Angiboust S. (2018) Deformation-enhanced fluid
917 and mass transfer along Western and Central Alps paleo-subduction interfaces:
918 Significance for carbon cycling models. *Geosphere* **14**, 2355–2375.

919 Johannes W. and Puhan D. (1971) The calcite-aragonite transition, reinvestigated.
920 *Contrib. Mineral. Petrol.* **31**, 28–38.

921 Kelemen P. B. and Manning C. E. (2015) Reevaluating carbon fluxes in
922 subduction zones, what goes down, mostly comes up. *Proc. Natl. Acad. Sci.*
923 *USA* **112**, E3997–E4006.

924 Kelley D. S., Karson J. A., Blackman D. K., Früh-Green G. L., Butterfield D. A.,
925 Lilley M. D., Olson E. J., Schrenk M. O., Roe K. K., Lebon G. T., Rivizzigno
926 P. and the AT3-60 Shipboard Party. (2001) An off-axis hydrothermal vent
927 field near the Mid-Atlantic Ridge at 30° N. *Nature* **412**, 145–149.

928 Kelley D. S., Karson J. A., Früh-Green G. L., Yoerger D. R., Shank T. M.,
929 Butterfield D. A., Hayes J. M., Schrenk M. O., Olson E. J., Proskurowski G.,
930 Jakuba M., Bradley A., Larson B., Ludwig K., Glickson D., Buckman K.,
931 Bradley A. S., Brazelton W. J., Roe K., Elend M. J., Delacour A., Bernasconi

- 932 S. M., Lilley M. D., Baross J. A., Summons R. E. and Sylva S. P. (2005) A
933 serpentinite-hosted ecosystem: The Lost City hydrothermal field. *Science* **307**,
934 1428–1434.
- 935 Klein F., Bach W. and McCollom T. M. (2013) Compositional controls on
936 hydrogen generation during serpentinization of ultramafic rocks. *Lithos* **178**,
937 55–69.
- 938 Klein F., Humphris S. E., Guo W., Schubotz F., Schwarzenbach E. M. and Orsi
939 W. D. (2015) Fluid mixing and the deep biosphere of a fossil Lost City-type
940 hydrothermal system at the Iberia Margin. *Proc. Natl. Acad. Sci. USA* **112**,
941 12036–12041.
- 942 Klein F., Grozeva N. G. and Seewald J. S. (2019) Abiotic methane synthesis and
943 serpentinization in olivine-hosted fluid inclusions. *Proc. Natl. Acad. Sci. USA*
944 **116**, 17666–17672.
- 945 Klein F., Tarnas J. D. and Bach W. (2020) Abiotic sources of molecular hydrogen
946 on Earth. *Elements* **16**, 19–24.
- 947 Lafay R., Baumgartner L. P., Stephane S., Suzanne P., German M. H. and Torsten
948 V. (2017) Petrologic and stable isotopic studies of a fossil hydrothermal
949 system in ultramafic environment (Chenaillet ophicalcites, Western Alps,
950 France): Processes of carbonate cementation. *Lithos* **294–295**, 319–338.
- 951 Lamadrid H. M., Rimstidt J. D., Schwarzenbach E. M., Klein F., Ulrich S.,
952 Dolocan A. and Bodnar R. J. (2017) Effect of water activity on rates of
953 serpentinization of olivine. *Nat. Commun.* **8**, 16107.
- 954 Lamadrid H. M., Zajacz Z., Klein F. and Bodnar R. J. (2021) Synthetic fluid
955 inclusions XXIII. Effect of temperature and fluid composition on rates of
956 serpentinization of olivine. *Geochim. Cosmochim. Acta* **292**, 285–308.
- 957 Lazar C. (2020) Using silica activity to model redox-dependent fluid
958 compositions in serpentinites from 100 to 700 °C and from 1 to 20 kbar. *J.*
959 *Petrol.* **61**, ega101.

- 960 Lazar C., Zhang C., Manning C. E. and Mysen B. O. (2014) Redox effects on
961 calcite–portlandite–fluid equilibria at forearc conditions: Carbon mobility,
962 methanogenesis, and reduction melting of calcite. *Am. Mineral.* **99**, 1604–
963 1615.
- 964 Li Y. (2017) Immiscible C–H–O fluids formed at subduction zone conditions.
965 *Geochem. Perspect. Lett.* **3**, 12–21.
- 966 Li X.-P., Zhang L., Wei C., Ai Y. and Chen J. (2007) Petrology of rodingite
967 derived from eclogite in western Tianshan, China. *J. Metamorph. Geol.* **25**,
968 363–382.
- 969 Li X.-P., Zhang L.-F., Wilde S. A., Song B. and Liu X.-M. (2010) Zircons from
970 rodingite in the Western Tianshan serpentinite complex: mineral chemistry
971 and U–Pb ages define nature and timing of rodingitization. *Lithos* **118**, 17–34.
- 972 Li J.-L., Klemd R., Gao J. and Meyer M. (2012) Coexisting carbonate-bearing
973 eclogite and blueschist in SW Tianshan, China: Petrology and phase equilibria.
974 *J. Asian Earth Sci.* **60**, 174–187.
- 975 Li J.-L., Klemd R., Gao J. and Meyer M. (2014) Compositional zoning in
976 dolomite from lawsonite-bearing eclogite (SW Tianshan, China): Evidence
977 for prograde metamorphism during subduction of oceanic crust. *Am. Mineral.*
978 **99**, 206–217.
- 979 Li X., Zhang L., Wei C., Slabunov A. I. and Bader T. (2018) Quartz and
980 orthopyroxene exsolution lamellae in clinopyroxene and the metamorphic *P*–
981 *T* path of Belomorian eclogites. *J. Metamorph. Geol.* **36**, 1–22.
- 982 Lin F., Bodnar R. J. and Becker S. P. (2007) Experimental determination of the
983 Raman CH₄ symmetric stretching (γ_1) band position from 1–650 bar and 0.3–
984 22 °C: Application to fluid inclusion studies. *Geochim. Cosmochim. Acta* **71**,
985 3746–3756.
- 986 Lin M., Zhang G., Li N., Li H. and Wang J. (2021) An improved *in situ* zircon
987 U–Pb dating method at high spatial resolution ($\leq 10 \mu\text{m}$ spot) by LA-MC-
988 ICP-MS and its application. *Geostand. Geoanal. Res.* **45**, 265–285.

- 989 Liou J. G., Tsujimori T., Zhang R. Y., Katayama I. and Maruyama S. (2004)
990 Global UHP metamorphism and continental subduction/collision: the
991 Himalayan model. *Int. Geol. Rev.* **46**, 1–27.
- 992 Lü Z. and Zhang L. (2012) Coesite in the eclogite and schist of the Atantayi Valley,
993 southwestern Tianshan, China. *Chinese Sci. Bull.* **57**, 1467–1472.
- 994 Lü Z., Bucher K., Zhang L. and Du J. (2012a) The Habutengsu metapelites and
995 metagreywackes in western Tianshan, China: metamorphic evolution and
996 tectonic implications. *J. Metamorph. Geol.* **30**, 907–926.
- 997 Lü Z., Zhang L., Du J., Yang X., Tian Z. and Xia B. (2012b) Petrology of HP
998 metamorphic veins in coesite-bearing eclogite from western Tianshan, China:
999 Fluid processes and elemental mobility during exhumation in a cold
1000 subduction zone. *Lithos* **136–139**, 168–186.
- 1001 Malvoisin B., Chopin C., Brunet F. and Galvez M. E. (2012) Low-temperature
1002 wollastonite formed by carbonate reduction: a marker of serpentinite redox
1003 conditions. *J. Petrol.* **53**, 159–176.
- 1004 McCollom T. M. and Bach W. (2009) Thermodynamic constraints on hydrogen
1005 generation during serpentinization of ultramafic rocks. *Geochim. Cosmochim.*
1006 *Acta* **73**, 856–875.
- 1007 McCollom T. M. and Seewald J. S. (2001) A reassessment of the potential for
1008 reduction of dissolved CO₂ to hydrocarbons during serpentinization of olivine.
1009 *Geochim. Cosmochim. Acta* **65**, 3769–3778.
- 1010 McCollom T. M. and Seewald J. S. (2013) Serpentinites, hydrogen, and life.
1011 *Elements* **9**, 129–134.
- 1012 McDermott J. M., Seewald J. S., German C. R. and Sylva S. P. (2015) Pathways
1013 for abiotic organic synthesis at submarine hydrothermal fields. *Proc. Natl.*
1014 *Acad. Sci. USA* **112**, 7668–7672.
- 1015 Ménez B. (2020) Abiotic hydrogen and methane: Flues for life. *Elements* **16**, 39–
1016 46.

- 1017 Mukhina E., Kolesnikov A. and Kutcherov V. (2017) The lower pT limit of deep
1018 hydrocarbon synthesis by CaCO₃ aqueous reduction. *Sci. Rep.* **7**, 5749.
- 1019 Peng W., Zhang L., Shen T. and Hu H. (2018) Implications for the deep carbon
1020 cycle from the carbonation in subduction zones: A case study of carbonated
1021 micaschists from Chinese southwestern Tianshan. *Acta Petrol. Sin.* **34**, 1204–
1022 1218.
- 1023 Peng W., Zhang L., Menzel M. D., Vitale Brovarone A., Tumiati S., Shen T. and
1024 Hu H. (2020) Multistage CO₂ sequestration in the subduction zone: Insights
1025 from exhumed carbonated serpentinites, SW Tianshan UHP belt, China.
1026 *Geochim. Cosmochim. Acta* **270**, 218–243.
- 1027 Penniston-Dorland S. C., Kohn M. J. and Manning C. E. (2015) The global range
1028 of subduction zone thermal structures from exhumed blueschists and eclogites:
1029 Rocks are hotter than models. *Earth Planet. Sci. Lett.* **428**, 243–254.
- 1030 Peretti A., Dubessy J., Mullis J., Frost B. R. and Trommsdorff V. (1992) Highly
1031 reducing conditions during Alpine metamorphism of the Malenco peridotite
1032 (Sondrio, northern Italy) indicated by mineral paragenesis and H₂ in fluid
1033 inclusions. *Contrib. Mineral. Petrol.* **112**, 329–340.
- 1034 Piccoli F., Vitale Brovarone A., Beyssac O., Martinez I., Ague J. J. and Chaduteau
1035 C. (2016) Carbonation by fluid–rock interactions at high-pressure conditions:
1036 Implications for carbon cycling in subduction zones. *Earth Planet. Sci. Lett.*
1037 **445**, 146–159.
- 1038 Piccoli F., Vitale Brovarone A. and Ague J. J. (2018) Field and petrological study
1039 of metasomatism and high-pressure carbonation from lawsonite eclogite-
1040 facies terrains, Alpine Corsica. *Lithos* **304–307**, 16–37.
- 1041 Plümper O., King H. E., Geisler T., Liu Y., Pabst S., Savov I. P., Rost D. and Zack
1042 T. (2017) Subduction zone forearc serpentinites as incubators for deep
1043 microbial life. *Proc. Natl. Acad. Sci. USA* **114**, 4324–4329.

- 1044 Proskurowski G., Lilley M. D., Seewald J. S., Früh-Green, G. L., Olson, E. J.,
1045 Lupton, J. E., Sylva, S. P. and Kelley, D. S. (2008) Abiogenic hydrocarbon
1046 production at Lost City hydrothermal field. *Science* **319**, 604–607.
- 1047 Ramos F. C., Wolff J. A. and Tollstrup D. L. (2004) Measuring $^{87}\text{Sr}/^{86}\text{Sr}$ variations
1048 in minerals and groundmass from basalts using LA-MC-ICPMS. *Chem. Geol.*
1049 **211**, 135–158.
- 1050 Robie R. A. and Hemingway B. S. (1995) *Thermodynamic properties of minerals*
1051 *and related substances at 298.15 K and 1 bar (10^5 Pascals) pressure and at*
1052 *higher temperatures*. U.S. Geological Survey Bulletin 2131.
- 1053 Sachan H. K., Mukherjee B. K. and Bodnar R. J. (2007) Preservation of methane
1054 generated during serpentinization of upper mantle rocks: Evidence from fluid
1055 inclusions in the Nidar ophiolite, Indus Suture Zone, Ladakh (India). *Earth*
1056 *Planet. Sci. Lett.* **257**, 47–59.
- 1057 Scambelluri M., Müntener O., Ottolini L., Pettke T. T. and Vannucci R. (2004)
1058 The fate of B, Cl and Li in the subducted oceanic mantle and in the antigorite
1059 breakdown fluids. *Earth Planet. Sci. Lett.* **222**, 217–234.
- 1060 Scambelluri M., Bebout G. E., Belmonte D., Gilio M., Campomenosi N., Collins
1061 N. and Crispini L. (2016) Carbonation of subduction-zone serpentinite (high-
1062 pressure ophi carbonate; Ligurian Western Alps) and implications for the deep
1063 carbon cycling. *Earth Planet. Sci. Lett.* **441**, 155–166.
- 1064 Schwarzenbach E. M., Früh-Green G. L., Bernasconi S. M., Alt J. C. and Plas A.
1065 (2013) Serpentinization and carbon sequestration: A study of two ancient
1066 peridotite-hosted hydrothermal systems. *Chem. Geol.* **351**, 115–133.
- 1067 Scicchitano M. R., Rubatto D., Hermann J., Shen T., Padrón-Navarta J. A.,
1068 Williams I. S. and Zheng Y.-F. (2018) *In situ* oxygen isotope determination
1069 in serpentine minerals by ion microprobe: reference materials and applications
1070 to ultrahigh-pressure serpentinites. *Geostand. Geoanal. Res.* **42**, 459–479.

- 1071 Sharma A., Cody G. D. and Hemley R. J. (2009) *In situ* diamond-anvil cell
1072 observations of methanogenesis at high pressures and temperatures. *Energ.*
1073 *Fuel.* **23**, 5571–5579.
- 1074 Sheik C. S., Cleaves II H. J., Johnson-Finn K., Giovannelli D., Kieft T. L.,
1075 Papineau D., Schrenk M. O. and Tumiati S. (2020) Abiotic and biotic
1076 processes that drive carboxylation and decarboxylation reactions. *Am.*
1077 *Mineral.* **105**, 609–615.
- 1078 Shen T., Zhang L. and Li X. (2012) Geochemical characteristics of rodingite
1079 derived from eclogite in western Tianshan, Xinjiang, China and its
1080 implications for subduction zone fluid. *Acta Petrol. Sin.* **28**, 2235–2249.
- 1081 Shen T., Hermann J., Zhang L., Lü Z., Padrón-Navarta J. A., Xia B. and Bader T.
1082 (2015) UHP metamorphism documented in Ti-chondrodite- and Ti-
1083 clinohumite-bearing serpentinitized ultramafic rocks from Chinese
1084 southwestern Tianshan. *J. Petrol.* **56**, 1425–1458.
- 1085 Shen T., Wu F., Zhang L., Hermann J., Li X. and Du J. (2016) In-situ U–Pb dating
1086 and Nd isotopic analysis of perovskite from a rodingite blackwall associated
1087 with UHP serpentinite from southwestern Tianshan, China. *Chem. Geol.* **431**,
1088 67–82.
- 1089 Shi G. U., Tropper P., Cui W., Tan J. and Wang C. (2005) Methane (CH₄)-bearing
1090 fluid inclusions in the Myanmar jadeitite. *Geochem. J.* **39**, 503–516.
- 1091 Sieber M. J., Hermann J. and Yaxley G. M. (2018) An experimental investigation
1092 of C–O–H fluid-driven carbonation of serpentinites under forearc conditions.
1093 *Earth Planet. Sci. Lett.* **496**, 178–188.
- 1094 Sieber M. J., Yaxley G. M. and Hermann J. (2020) Investigation of fluid-driven
1095 carbonation of a hydrated, forearc mantle wedge using serpentinite cores in
1096 high-pressure experiments. *J. Petrol.* **61**, egaa035.
- 1097 Song S., Su L., Niu Y., Lai Y. and Zhang L. (2009) CH₄ inclusions in orogenic
1098 harzburgite: Evidence for reduced slab fluids and implication for redox
1099 melting in mantle wedge. *Geochim. Cosmochim. Acta* **73**, 1737–1754.

- 1100 Steele-MacInnis M., Lecumberri-Sanchez P. and Bodnar R. J. (2012)
1101 HOKIEFLINCS_H₂O-NaCl: A Microsoft Excel spreadsheet for interpreting
1102 microthermometric data from fluid inclusions based on the *PVTX* properties
1103 of H₂O–NaCl. *Comput. Geosci.* **49**, 334–337.
- 1104 Syracuse E. M., van Keken P. E. and Abers G. A. (2010) The global range of
1105 subduction zone thermal models. *Phys. Earth Planet. In.* **183**, 73–90.
- 1106 Tan Z., Agard P., Gao J., John T., Li J., Jiang T., Bayet L., Wang X. and Zhang
1107 X. (2017) P–T–time–isotopic evolution of coesite-bearing eclogites:
1108 Implications for exhumation processes in SW Tianshan. *Lithos* **278–281**, 1–
1109 25.
- 1110 Tao R., Zhang L., Fei Y. and Liu Q. (2014) The effect of Fe on the stability of
1111 dolomite at high pressure: Experimental study and petrological observation in
1112 eclogite from southwestern Tianshan, China. *Geochim. Cosmochim. Acta* **143**,
1113 253–267.
- 1114 Tao R., Zhang L., Tian M., Zhu J., Liu X., Liu J., Höfer H. E., Stagno V. and Fei
1115 Y. (2018a) Formation of abiotic hydrocarbon from reduction of carbonate in
1116 subduction zones: Constraints from petrological observation and experimental
1117 simulation. *Geochim. Cosmochim. Acta* **239**, 390–408.
- 1118 Tao R., Zhang L., Li S., Zhu J. and Ke S. (2018b) Significant contrast in the Mg-
1119 C-O isotopes of carbonate between carbonated eclogite and marble from the
1120 S.W. Tianshan UHP subduction zone: Evidence for two sources of recycled
1121 carbon. *Chem. Geol.* **483**, 65–77.
- 1122 Tian Z. L. and Wei C. J. (2013) Metamorphism of ultrahigh-pressure eclogites
1123 from the Kebuerte Valley, South Tianshan, NW China: phase equilibria and
1124 *P–T* path. *J. Metamorph. Geol* **31**, 281–300.
- 1125 Truche L., McCollom T. M. and Martinez I. (2020) Hydrogen and abiotic
1126 hydrocarbons: Molecules that change the world. *Elements* **16**, 13–18.

- 1127 Tumiati S. and Malaspina N. (2019) Redox processes and the role of carbon-
1128 bearing volatiles from the slab–mantle interface to the mantle wedge. *J. Geol.*
1129 *Soc.* **176**, 388–397.
- 1130 Tumiati S., Fumagalli P., Tiraboschi C. and Poli S. (2013) An experimental study
1131 on COH-bearing peridotite up to 3.2 GPa and implications for crust–mantle
1132 recycling. *J. Petrol.* **54**, 453–479.
- 1133 Tumiati S., Tiraboschi C., Sverjensky D. A., Pettke T., Recchia S., Ulmer P.,
1134 Miozzi F. and Poli S. (2017) Silicate dissolution boosts the CO₂
1135 concentrations in subduction fluids. *Nat. Commun.* **8**, 616.
- 1136 Tumiati S., Tiraboschi C., Miozzi F., Vitale-Brovarone A., Manning C. E.,
1137 Sverjensky D. A., Milani S. and Poli S. (2020) Dissolution susceptibility of
1138 glass-like carbon versus crystalline graphite in high-pressure aqueous fluids
1139 and implications for the behavior of organic matter in subduction zones.
1140 *Geochim. Cosmochim. Acta* **273**, 383–402.
- 1141 Ueno Y., Yamada K., Yoshida N., Maruyama S. and Isozaki Y. (2006) Evidence
1142 from fluid inclusions for microbial methanogenesis in the early Archaean era.
1143 *Nature* **440**, 516–519.
- 1144 van der Straaten F., Halama R., John T., Schenk V., Hauff F. and Andersen N.
1145 (2012) Tracing the effects of high-pressure metasomatic fluids and seawater
1146 alteration in blueschist-facies overprinted eclogites: Implications for
1147 subduction channel processes. *Chem. Geol.* **292–293**, 69–87.
- 1148 Veizer J., Ala D., Azmy K., Bruckschen P., Buhl D., Bruhn F., Carden G. A. F.,
1149 Diener A., Ebner S., Godderis Y., Jasper T., Korte C., Pawellek, F., Podlaha
1150 O. G. and Strauss H. (1999) ⁸⁷Sr/⁸⁶Sr, δ¹³C and δ¹⁸O evolution of Phanerozoic
1151 seawater. *Chem. Geol.* **161**, 59–88.
- 1152 Vitale Brovarone A., Martinez I., Elmaleh A., Compagnoni R., Chaduteau C.,
1153 Ferraris C. and Esteve I. (2017) Massive production of abiotic methane during
1154 subduction evidenced in metamorphosed ophicarbonates from the Italian Alps.
1155 *Nat. Commun.* **8**, 14134.

- 1156 Vitale Brovarone A., Sverjensky D. A., Piccoli F., Ressico F., Giovannelli D. and
1157 Daniel I. (2020) Subduction hides high-pressure sources of energy that may
1158 feed the deep subsurface biosphere. *Nat. Commun.* **11**, 3880.
- 1159 Vroon P. Z., van der Wagt B., Koornneef J. M. and Davies G. R. (2008) Problems
1160 in obtaining precise and accurate Sr isotope analysis from geological materials
1161 using laser ablation MC-ICPMS. *Anal. Bioanal. Chem.* **390**, 465–476.
- 1162 Wheat C. G., Seewald J. S. and Takai K. (2020) Fluid transport and reaction
1163 processes within a serpentinite mud volcano: South Chamorro Seamount.
1164 *Geochim. Cosmochim. Acta* **269**, 413–428.
- 1165 Whitney D. L. and Evans B. W. (2010) Abbreviations for names of rock-forming
1166 minerals. *Am. Mineral.* **95**, 185–187.
- 1167 Woodhead J., Swearer S., Hergt J. and Maas R. (2005) *In situ* Sr-isotope analysis
1168 of carbonates by LA-MC-ICP-MS: interference corrections, high spatial
1169 resolution and an example from otolith studies. *J. Anal. At. Spectrom.* **20**, 22–
1170 27.
- 1171 Xia B., Zhang L., Xia Y. and Bader T. (2014) The tectonic evolution of the
1172 Tianshan Orogenic Belt: Evidence from U–Pb dating of detrital zircons from
1173 the Chinese southwestern Tianshan accretionary mélange. *Gondwana Res.* **25**,
1174 1627–1643.
- 1175 Xu H., Zhao Y., Vogel S. C., Daemen L. L. and Hickmott D. D. (2007)
1176 Anisotropic thermal expansion and hydrogen bonding behavior of portlandite:
1177 A high-temperature neutron diffraction study. *J. Solid State Chem.* **180**, 1519–
1178 1525.
- 1179 Yang Y., Wu F., Xie L., Yang J. and Zhang Y. (2009) In-situ Sr isotopic
1180 measurement of natural geological samples by LA-MC-ICP-MS. *Acta Petrol.*
1181 *Sin.* **25**, 3431–3441.
- 1182 Yang C., Ni Z., Wang T., Chen Z., Hong H., Wen L., Luo B. and Wang W. (2018)
1183 A new genetic mechanism of natural gas accumulation. *Sci. Rep.* **8**, 8336.

- 1184 Zhang L., Du J., Lü Z., Yang X., Gou L., Xia B., Chen Z., Wei C. and Song S.
1185 (2013) A huge oceanic-type UHP metamorphic belt in southwestern Tianshan,
1186 China: Peak metamorphic age and P – T path. *Chinese Sci. Bull.* **58**, 4378–4383.
- 1187 Zhang L., Wang Y., Zhang L. and Lü Z. (2019) Ultrahigh pressure metamorphism
1188 and tectonic evolution of southwestern Tianshan orogenic belt, China: a
1189 comprehensive review. In *HP–UHP Metamorphism and Tectonic Evolution*
1190 *of Orogenic Belts* (eds. L. Zhang, Z. Zhang, H.-P. Schertl and C. Wei).
1191 Geological Society, London, Special Publications. pp. 133–152.
- 1192 Zhang L., Wang Q., Ding X. and Li W.-C. (2021) Diverse serpentinization and
1193 associated abiotic methanogenesis within multiple types of olivine-hosted
1194 fluid inclusions in orogenic peridotite from northern Tibet. *Geochim.*
1195 *Cosmochim. Acta* **296**, 1–17.
- 1196 Zhu J., Zhang L., Lü Z. and Bader T. (2018) Elemental and isotopic (C, O, Sr, Nd)
1197 compositions of Late Paleozoic carbonated eclogite and marble from the SW
1198 Tianshan UHP belt, NW China: Implications for deep carbon cycle. *J. Asian*
1199 *Earth Sci.* **153**, 307–324.
- 1200 Zhu J., Zhang L., Tao R. and Fei Y. (2020) The formation of graphite-rich eclogite
1201 vein in S.W. Tianshan (China) and its implication for deep carbon cycling in
1202 subduction zone. *Chem. Geol.* **533**, 119430.

1203

1204 **FIGURE CAPTIONS**

1205 **Fig. 1.** Geological background of the Chinese southwestern Tianshan. (A)
1206 Simplified tectonic framework of the western part of the Chinese Tianshan
1207 (modified from [Tian and Wei, 2013](#)). (B) Schematic geological map of the
1208 Chinese southwestern Tianshan HP–UHP metamorphic belt (modified from
1209 [Zhang et al., 2013](#)). Grey stars show sample localities of CH₄-bearing carbonated
1210 eclogites at Kebuerte and Habutengsu in the metamorphic belt ([Tao et al., 2018a](#)).
1211 (C) Detailed geological map of Changawuzi showing the sample locality of CH₄-
1212 bearing ophidolomites in this study (modified from [Shen et al., 2015](#)).

1213

1214 **Fig. 2.** Petrological characteristics of the studied ophidolomites. (A and B)
1215 Discontinuous and folded dolomite veins (with the rim encircled by yellowish
1216 calcite and brucite) filling the host serpentinites (hand-specimen scale). (C and D)
1217 Dolomite growth at the expense of antigorite, with unreacted antigorite visible
1218 (cross-polarized light). In some cases, antigorite shows abnormal interference
1219 colors due to the thick sections. (E and F) Decomposition of dolomite into cloudy
1220 calcite and brucite (cross-polarized light). (G) Back-scattered electron image (the
1221 upper part) and compositional X-ray map (the lower part) of dolomite
1222 decomposition into calcite–brucite intergrowths. The newly grown calcite and
1223 brucite extend into the inner parts of dolomite along microcracks. (H) The
1224 enlargement of the box in (G) showing intergrowths of acicular calcite and brucite
1225 and patches of relict dolomite in calcite. Mineral abbreviations in this study follow
1226 [Whitney and Evans \(2010\)](#).

1227

1228 **Fig. 3.** Occurrence of olivine and microstructures of magnetite-hosted mineral
1229 inclusions in the studied ophidolomites. (A) Olivine relicts in the antigorite matrix.
1230 (B) Coarse magnetite grains enclosing abundant minerals in the matrix of
1231 antigorite and dolomite. (C) Olivine in association with antigorite and brucite in
1232 magnetite. (D) Calcite and brucite growth at the expense of dolomite in magnetite,
1233 with dolomite relicts visible.

1234

1235 **Fig. 4.** Petrographic characteristics of fluid inclusions in the studied
1236 ophidolomites. (A and B) Type-I two-phase (vapor and liquid) fluid inclusions in
1237 dolomite. (C and D) Type-II single-phase fluid inclusions in dolomite. (E–G)
1238 Type-I two-phase (vapor and liquid) fluid inclusions in calcite intergrown with
1239 brucite.

1240

1241 **Fig. 5.** Raman spectra of fluid inclusions in the studied ophidolomites. (A and B)
1242 Type-I CH₄-bearing aqueous fluid inclusions in dolomite (A) and calcite
1243 intergrown with brucite (B). The strong fluorescence of the host carbonates
1244 sometimes prevents conclusive Raman investigation of the liquid phase of H₂O.
1245 (C) Type-II CH₄ ± H₂-bearing fluid inclusions in dolomite. Weaker but crucial
1246 peaks are enlarged. Scale bars of the close-up images are 10 μm.

1247

1248 **Fig. 6.** Isotope compositions of the studied ophidolomites. (A) *In situ* Sr isotope
1249 compositions of dolomite and calcite. The sky blue and purple dashed lines show
1250 ⁸⁷Sr/⁸⁶Sr ratios of the Tianshan HP ophidolomites and their dolomite separates
1251 (Peng et al., 2020) and the Ordovician–Carboniferous seawater (Veizer et al.,
1252 1999), respectively. The Tianshan UHP serpentinites are marine-originated (Shen
1253 et al., 2015) and have largely inherited Sr isotope compositions of the seawater
1254 (Peng et al., 2020). The sky blue and purple solid lines show the average ⁸⁷Sr/⁸⁶Sr
1255 ratios of dolomite and calcite, respectively. Error bars represent the 2σ internal
1256 precision. (B) C and O isotope compositions of dolomite and calcite. For
1257 comparison, δ¹³C and δ¹⁸O of carbonates in various lithologies from the Chinese
1258 southwestern Tianshan are plotted (van der Straaten et al., 2012; Collins et al.,
1259 2015; Peng et al., 2018, 2020; Zhu et al., 2018). The green and grey areas display
1260 δ¹³C of marine carbonates (Hoefs, 2009) and carbonates in CH₄-bearing
1261 ophicalcites from the Western Alps (Vitale Brovarone et al., 2017), respectively.
1262 The black and blue solid lines correspond to C isotopic trends of carbonates
1263 affected by decarbonation and carbonate reduction from Galvez et al. (2013b),
1264 while the black and blue dashed lines represent the possible trends of
1265 decarbonation and carbonate reduction in the Tianshan. Uncertainties of values
1266 are smaller than the symbol sizes.

1267

1268 **Fig. 7.** (A) Stabilities of phases under variable *f*O₂–*f*H₂ conditions in the Ca–Mg–
1269 C–O–H system (with fixed Ca:Mg:C of 1:1:2 in molar ratio) at 8 kbar and 420 °C.

1270 The orange dashed lines show $\log f_{\text{O}_2}$ of magnetite–hematite (MH), fayalite–
1271 magnetite–quartz (FMQ), and iron–magnetite (IM) buffers calculated at 8 kbar
1272 and 420 °C. The pink solid line represents the thermodynamically calculated
1273 model of slightly reduced H₂O at $X_{\text{O}} = 0.33 \sim 1/3$ in the H–O system (star: $X_{\text{O}} =$
1274 0.33333323 , corresponding to $y_{\text{H}_2\text{O}} = 0.999995$ and $y_{\text{H}_2} = 0.000005$). (B) The P – T
1275 pseudosection displaying diverse phase assemblages in the Ca–Fe–Mg–Si–C–O–
1276 H system at $\log f_{\text{O}_2} = -26.0$ and $\log f_{\text{H}_2} = 0.8$. The rectangle confines P – T
1277 conditions for the onset of retrograde serpentinization in the Tianshan (7–9 kbar
1278 and 410–430 °C; [Li et al., 2007, 2010](#)).

1279

1280 **Fig. 8.** P – T diagram showing stages of dolomite reduction and fluid entrapment
1281 during exhumation of the Chinese southwestern Tianshan. Stage A represents the
1282 onset of dolomite reduction, inferred from retrograde serpentinization starting at
1283 7–9 kbar and 410–430 °C and propagating to lower P – T conditions (Stage B) in
1284 the Tianshan ([Li et al., 2007, 2010](#)). Solid lines marked with 1, 2, and 3 display
1285 the controversial P – T conditions for the chrysotile to antigorite transition from [Li](#)
1286 [et al. \(2007, 2010\)](#), [Scambelluri et al. \(2004\)](#), and [Evans et al. \(1976\)](#), respectively,
1287 resulting in uncertainties of Stage B. The constrained P – T conditions for fluid
1288 entrapment (Stage C) are based on the fluid inclusion isochores intersecting the
1289 retrograde P – T path of the Tianshan ([Tan et al., 2017](#)). The stability fields of
1290 lizardite, antigorite, and olivine, as well as the main transformation reactions and
1291 cold subduction gradient, are from [Guillot et al. \(2015\)](#). The calcite to aragonite
1292 transition is from [Johannes and Puhan \(1971\)](#).

1293

1294 **Fig. 9.** (A) Summary of abiogenic CH₄ formation through dolomite reduction in
1295 ophidolomites during exhumation of the Chinese southwestern Tianshan. The P –
1296 T constraints for HP ophidolomites in the Tianshan are from [Peng et al. \(2020\)](#).
1297 The red rectangle [T] displays P – T conditions for the onset of dolomite reduction,
1298 inferred from retrograde serpentinization in the Tianshan ([Li et al., 2007, 2010](#)).

1299 For comparison, P – T estimates for carbonate reduction during shallow subduction
1300 in Alpine Corsica [C] ([Malvoison et al., 2012](#); [Galvez et al., 2013a, b](#)) and the
1301 Italian Alps [A] ([Vitale Brovarone et al., 2017](#); [Giuntoli et al., 2020](#)) are shown.
1302 The P – T path of the Tianshan is from [Tan et al. \(2017\)](#). The cyan and light cyan
1303 areas represent the modelled prograde P – T paths of subduction zones at the slab
1304 interface and slab Moho (7 km beneath the slab surface; [Syracuse et al., 2010](#)),
1305 respectively. The sky blue solid curve (PD) shows the global average range of
1306 prograde P – T paths from subduction-related metamorphic rocks ([Penniston-
1307 Dorland et al., 2015](#)). Facies boundaries and abbreviations are from [Liou et al.
1308 \(2004\)](#). (B) General model showing abiotic CH_4 production through dolomite
1309 reduction during shallow subduction. Due to uncertainties in the scale and extent
1310 of serpentinization in subducted slabs ([Li et al., 2007, 2010](#); [Vitale Brovarone et
1311 al., 2017, 2020](#); [Lazar, 2020](#)), dashed arrow lines represent fluid migration
1312 pathways instead of the steady fluid flow. The extent of alteration is dependent on
1313 the infiltration of the reactive reduced fluids. Possible CH_4 – H_2 -generating
1314 reactions are listed but without stoichiometric numbers. Figure is not to scale.